Mineralizations and transition metal mobility driven by organic carbon during low-temperature serpentinization

Bénédicte Ménez, Valerio Pasini, François Guyot, Karim Benzerara, Sylvain Bernard, Daniele Brunelli

Mineralizations and transition metal mobility driven by organic carbon during low-temperature serpentinization

Bénédicte Ménez [a,*], Valerio Pasini [a,b,#], Francois Guyot [c], Karim Benzerara [c], Sylvain Bernard [c], Daniele Brunelli [b,d]

[a] *Institut de Physique du Globe de Paris, Sorbonne Paris Cité, Univ. Paris Diderot, UMR CNRS 7154, 1 rue Jussieu, 75238 Paris cedex 05, France*

[b] *Dipartimento di Scienze Chimiche e Geologiche, Università di Modena e Reggio Emilia, Via Campi 103, 41125 Modena, Italy*

[c] *Sorbonne Université, Muséum National d'Histoire Naturelle, UMR CNRS 7590, IRD, Institut de Minéralogie, de Physique des Matériaux et de Cosmochimie, 4 place Jussieu, 75005 Paris, France*

[d] *Istituto di Scienze del Mare-CNR, Via Gobetti 101, 49100 Bologna, Italy*

* Corresponding author at: Institut de Physique du Globe de Paris, 1 rue Jussieu, 75238 Paris cedex 05, France

E-mail address: menez@ipgp.fr (B. Ménez)

[#] now at SRA Instruments SpA, Via Alla Castellana 3, 20063 Cernusco sul Naviglio, Italy

Revised version Lithos – July 2018

Abbreviations:

bast bastite

C-XANES X-ray absorption near edge structure at the carbon K-edge

EDXS energy dispersive X-ray spectrometry

EMPA electron microprobe analysis

EPS extracellular polymeric substances

Fe-ox iron oxide

FIB focused ion beam

H-adr andraditic hydrogarnet

HAADF-STEM high-angle annular dark-field scanning transmission electron microscopy

HR-TEM high resolution transmission electron microscopy

pol-spt polygonal and polyhedral serpentine

SAED selected area electron diffraction

SEM scanning electron microscopy

spl spinel

spt serpentine

STEM scanning transmission electron microscopy

STXM scanning transmission X-ray microscopy

TEM transmission electron microscopy

ABSTRACT

Serpentinization is known to provide substantial amounts of energy in the form of molecular hydrogen along with a suite of abiotic organic compounds of low molecular weight (mainly as short chain alkanes and carboxylic acids), all sustaining the development of microbial ecosystems in the mantle-derived crust. The latter have a cryptoendolithic life style and are responsible for (i) the local formation of biomass and of organic metabolic byproducts and (ii) the production of extracellular polymeric substances which organize the community in the form of a biofilm at the surface of the rock-forming minerals. In accordance, whatever their origin, organic compounds can be diverse and widespread in the shallow oceanic crust where they undergo hydrothermal degradation and remobilization through fluid circulations. Here we show that organic carbon is directly involved in low temperature serpentinization reactions (< 200°C). Fine scale investigations of microbial niches hosted in serpentinites from the Mid-Atlantic ridge were performed using scanning and transmission electron microscopy along with scanning transmission X-ray microscopy. They suggest that organic films generated at mineral surfaces as a consequence of rock colonization may influence the nature and structure of the serpentinization products as well as the mobility and speciation of transition metals as the reaction progresses. This likely constitutes an efficient yet poorly considered mechanism in active serpentinizing systems with possible implications for ore formation associated with the alteration of ophiolitic massifs and subsurface storage.

Keywords: serpentinization; ; mid-ocean ridges; organic carbon; metal mobility; organomineralization; supergene ore formation

1. Introduction

It was long assumed that the net flux of most hydrothermally-derived metals to the ocean was negligible because abundant polymetallic particulate phases, predominantly in the form of Fe-sulfides and Fe-oxyhydroxides, form when vent fluids discharge at the seafloor (German et al., 1991; Mottl and McConachy, 1990). Nonetheless, the importance of hydrothermally-derived metals for ocean biogeochemistry has been revisited during the last two decades. Enrichments in dissolved iron compared to predicted solubility values were reported in non-buoyant hydrothermal plumes, suggesting that a fraction of metals escapes from precipitation (Field and Sherrell, 2000; Resing et al., 2015; Statham et al., 2005). Organic compounds were shown to bind and stabilize dissolved metals (Bennet et al., 2008; Hawkes et al., 2013; Sander and Koschinsky, 2011; Toner et al., 2009) or solid sulfur and iron particles (Fitzsimmons et al., 2017; Klevenz et al., 2011; Lau and Hsu-Kim, 2008), overall facilitating their long-range oceanic transport (Fitzsimmons et al., 2017; Sander and Koschinsky, 2011; Sands et al., 2012; Wu et al., 2011). Organic-metal complexation reduces the reactivity of the metallic species and prevents metal redox changes, precipitation or scavenging into or onto particulate phases (Bennett et al., 2008). Therefore, it significantly increases dissolved metal concentrations in hydrothermal fluids and associated fluxes of metals to the global ocean (Resing et al., 2015; Sander and Koschinsky, 2011). Although iron has been one of the most investigated metals due to its role as a limiting nutrient (Bennet et al., 2008; Boyd and Ellwood, 2010; Sander and Koschinsky, 2011; Toner et al., 2009), hydrothermally-derived chromium, copper, and manganese have also been shown to be transported to the non-buoyant hydrothermal plume and across oceans as complexes stabilized with organic ligands (Fitzsimmons et al., 2017; Resing et al., 2015; Sander et al., 2007).

While their compositions and sources are not fully determined, these metal-stabilizing organic complexes are postulated to form from organic ligands available in excess in the plume source regions (Bennett et al., 2008, 2011). In addition to the small fraction of thermally-reworked marine dissolved and particulate organic matter that outlived hydrothermal circulation (Hawkes et

al., 2015; Rossel et al., 2017) and organic compounds mobilized during hydrothermal alteration of organic carbon-rich sediments (e.g., Kawka and Simoneit, 1987), these plume enrichments in organic matter were postulated to derive from (i) chemosynthetic microbial activities occurring at or close to vents (Lang et al., 2006), (ii) hydrothermal degradation of vent-hosted biological material (Simoneit et al., 2004) and (iii) abiotic hydrothermal synthesis (Konn et al., 2015 and references therein). All these processes form a large diversity of organic compounds pervasively entrained into buoyant hydrothermal plumes through chimney venting or diffuse flow. However, life is not limited to ocean, sediment or seafloor hydrothermal vent ecosystems and both the ultramafic and mafic oceanic subseafloors were also recognized as potentially-large microbial habitats (Mason et al., 2010; Ménez et al., 2012; Santelli et al., 2008). In particular, the serpentinization of mantle-derived rocks is known to provide substantial amounts of molecular hydrogen through the reduction of water coupled to the oxidation of ferrous iron-bearing minerals. This in turn favors the formation of organic compounds such as short chain alkanes and carboxylic acids. Together with molecular hydrogen, these organic compounds provide, despite the alkaline pHs associated with serpentinization reactions, valuable energy sources for the development of cryptoendolithic microbial ecosystems in the mantle-derived crust (Schrenk et al., 2013). These ecosystems can locally form biomass and organic metabolic byproducts along with extracellular polymeric substances (EPS) allowing to organize the community in the form of a biofilm at the surface of the rock-forming minerals. Abiotic organic synthesis and biological metabolic activities thus coexist in these environments, the complex interplay between both pathways during the multistage hydrothermal alteration of the oceanic crust being however far from being understood. In accordance, organic compounds can be diverse in origin and nature and pervasively present in the shallow oceanic crust where they undergo hydrothermal degradation and remobilization through fluid circulations (Pasini et al., 2013). Serpentinization reactions also affect redox-sensitive transition metals resulting in the formation of oxides, sulfides, native elements and alloys, depending on the chemical and physical conditions of the system. Organic complexation may also impact the fate of metals at depth in the oceanic lithosphere and play a role during fluid-rock

interactions that has never been considered yet.

Ménez et al. (2012) provided evidence for cobalt enrichments associated with the presence of carbon-rich phases in a serpentinite from the equatorial Mid-Atlantic Ridge (MAR). These organic phases were inherited, at least partly, from the presence of former ecosystems identified through remnants of complex organic molecules. The organic phases were also suggested to mediate the formation of polygonal and polyhedral serpentines (pol-spt) precipitating in the cavities of andraditic hydrogarnets (H-adr). Overall, this suggested a potential role of organic compounds in the regulation of elemental fluxes in the serpentinizing oceanic lithosphere. Here, we further investigate the occurrences of polyhedral and polygonal serpentine along with organic-metal associations in this MAR serpentinite by using a suite of high-resolution techniques, which includes electron microprobe analysis (EMPA), scanning and transmission electron microscopies (SEM and TEM) coupled with energy dispersive X-ray spectrometry (EDXS), scanning transmission electron microscopy (STEM), and scanning transmission X-ray microscopy (STXM) associated with X-ray absorption near edge structure at the carbon K-edge (C-XANES). The spatially-resolved characterization of transition metals and organic carbon down to the nanometer scale highlights (i) the involvement of an organic gel in the formation of pol-spt, (ii) a differential distribution of metals depending on the nature of the associated organic phases and (iii) the precipitation of nanometer-sized metallic oxides within the organic phases.

2. Material and methods

2.1. Geological setting

The studied rock was dredged during the joint Russian-Italian cruise S22 (*R/V Akademik Nikolaj Strakhov*) in the vicinity of the Sierra Leone area, a magma starved, slow-spreading region of the equatorial MAR at 5-7° N (Figs. 1a-b). The non-transform Sierra Leone fault is located between the Bogdanov and the Strakhov fracture zones (7°10’ N and 4° N, respectively). The rift

zone is morphologically characterized by isolated basins, tectonically separated by transverse uplifts (3000-2100 meters below seafloor) made up by outcrops of tectonized and altered deep-seated gabbros and mantle rocks (Peyve et al., 2003; Sharkov et al., 2012). Sample S2232-17 was collected on one of the most elevated blocks during the dredge haul S2232, which was carried out on an unsedimented ridge flanks of crust aged < 1 My (dredging interval: 6°08.9' N-33°25.4' W-6°09.1' N-33°25.4' from 2250 to 2000 meters below seafloor). About 200 kg of variably serpentinized peridotites were recovered during this haul (Peive et al., 2003).

2.2. Sample petrography

The studied rock corresponds to a fully serpentinized peridotite similar to rocks usually found in serpentinized mantle along Mid-Ocean ridges. Primary mineralogy has been tentatively inferred on the basis of the isomorphic mineral substitution. Prior to serpentinization, the rock primarily consisted in olivine + orthopyroxene + clinopyroxene + chromian-aluminous spinel revealing a spinel field equilibrated harzburgite (with theoretical modal clinopyroxene < 1%). Only few relics of those primary minerals can be found. They include clinopyroxenes, partially-preserved chromite cores derived from the chromian-aluminous spinel and rare olivine kernels (Pasini, 2013). As shown in Fig. 1c, the high temperature (> 200°C; Klein et al., 2014) hydrated paragenesis is composed of lizardite and magnetite, both after olivine, forming a characteristic mesh texture. Serpentine after olivine is also found around spinel remnants. Fine-grained lizardite, commonly defined as bastite, pseudomorphically replaces orthopyroxene. Chains or clusters of subhedral microgeode-like andraditic hydrogarnets (10-40 μm in size) are crystallized in, or very close to, the bastitized orthopyroxene along exsolution lamellae or microfractures (Fig. 1d). They are locally stretched or, alternatively, coalesce with one another and are often associated with iron oxides. H-adr are commonly found in serpentinites and usually grow over bastite under high pH and high Ca^{2+} activity, low O_2 fugacity, low silica activity and temperature below 200°C (Frost and Beard, 2007 and references therein; Plümper et al., 2014). Late serpentine veins of millimeter widths crosscut

the whole rock, attesting for several stages of serpentinization (Fig. 1c).

2.3. Sample preparation

Conventional petrographic thin sections were prepared for EMPA. SEM observations were performed on both silicon carbide-polished and unpolished, resin-free chips of sawn rock. TEM and STXM require electron and X-ray transparent samples, respectively, i.e., measuring at least less than ~100 nm in thickness. For this purpose, ultrathin focused ion beam (FIB) sections were milled using the FIB dual beam facility FEI Strata DB 235 operating at the IEMN (Lille, France). Resin-free chips were beforehand coated with gold in order to reinforce the protection of the surface and limit ion implantation into the samples. Regions of interest were covered with a platinum strap and then excavated from both side of the Pt strap using a 30 kV Ga^+ beam, emitted from a Ga liquid metal ion source operating at 7 to 1 nA. Further thinning to few tens of nanometers was obtained with a glancing angle beam at low current (~100 pA). FIB foils have been repeatedly used to study organic compounds within rocks with limited damages (e.g., Bassim et al., 2012; Benzerara et al., 2005; Bernard et al., 2009; Lepot et al., 2009).

2.4. Electron microscopy

SEM observations were performed on Au-coated, polished and unpolished, resin-free chips using a Zeiss SUPRA 55 VP field emission microscope (Service Commun de Microscopie Electronique à Balayage, UPMC, Paris, France). Beam accelerating voltage ranged between 15 kV (for backscattered electron images, microanalyses and chemical maps) and 1 kV (for high resolution secondary electron images). Images were collected using secondary electron detectors (Everhart-Thornley or InLens) and a backscattered electron detector (AsB). EDXS analyses were carried out with a PGT Sahara spectrometer. Chemical maps were acquired and processed using the Spirit® software. Spectra were fitted at each hyperspectral map point to produce elemental distributions.

TEM observations, high resolution-transmission electron microscopy (HR-TEM) and selected area electron diffraction (SAED) were performed on ultrathin FIB sections using JEOL 2100 microscopes operating at an accelerating voltage of 200 kV (IMPMC, Paris, France and Centro Interdipartimentale Grandi Strumenti, Modena, Italy). Both microscopes are equipped with a LaB_6 filament. EDXS analyses were performed using a JEOL detector at IMPMC and an Oxford INCA 100 detector at CIGS.

TEM images and STEM maps were also acquired on ultrathin FIB sections using a JEOL 2100F microscope equipped with a field effect gun and operating at 200 kV (IMPMC, Paris, France). High-angle annular dark-field (HAADF)-STEM was used with a focused electron beam of ~1 nm for Z-contrast imaging (Z referring to the atomic number). STEM-EDXS analyses were performed using a JEOL detector equipped with an ultrathin window allowing the detection of low-Z elements.

When necessary, SEM and TEM images were further processed with the ImageJ software (Schneider et al., 2012) for contrast and brightness adjustment.

2.5. Electron microprobe analysis

EMPA were performed on carbon-coated petrographic thin sections using the Cameca SXFive installed at CAMPARIS (Université Pierre et Marie Curie, Paris, France). Operating conditions were 10 kV and ~10 nA. Analyses were acquired in punctual mode.

2.6. Synchrotron-based scanning transmission X-ray microscopy

STXM and associated C-XANES analyses were performed at the branch line 5.3.2.2 (STXM Polymer beamline; Kilcoyne et al., 2003) of the Advanced Light Source (Lawrence Berkeley National Laboratory, USA). A zone plate was used to monochromatize and focus the X-ray beam produced by the synchrotron radiation to a spot size of ~25 nm. The ultrathin FIB foils

were scanned in the *x*-*y* directions at fixed photon energy to produce 2D images. The *x*-*y* plane refers to the plane perpendicular to the incident X-ray beam direction. The transmitted X-rays were detected a few hundreds of microns behind the sample. Energy calibration was carried out using the well-resolved peak of gaseous CO_2 at 294.96 eV. Carbon speciation maps with a 90 nm spatial resolution were acquired under He atmosphere by collecting image stacks over the energy range 275-340 eV with a theoretical energy resolution of ~0.1 eV. Counting time was 1 ms per image. The image contrast results from differential absorption of X-rays, which depends on the chemical composition of the sample. Images stacks were aligned using two dimensional cross correlation and processed using STACKLab, a Matlab© STXM data analysis script collection. This routine was also used to process energy-filtered images and extract XANES spectra at the carbon K-edge in order to document the bonding environment of carbon for the pixels of interest.

3. Results

3.1. Polyhedral and polygonal serpentine formation from hydrogarnet dissolution mediated by an organic gel

Euhedral dissolution pits are often found as piercing the surface of the andraditic hydrogarnets present in the S2232-17 serpentinite as shown by SEM (Fig. 2a) also highlighting large cavities inside H-adr (Supplementary Fig. 1). This suggests that dissolution process affected the hydrogarnets, as also proposed by Ménez et al. (2012). EMPA provided for H-adr a mean formula of $Ca_{2.71}(Fe_{1.61}^{3+},Ti_{0.01},Al_{0.17},Cr_{0.03},Mg_{0.02})(Si_{2.92}O_{10.93})(OH)_{1.07}$ (Supplementary Table 1). Pits and cavities are filled by polyhedral serpentine spheroids and polygonal serpentine rods (pol-spt), both showing a wide size range (few tens to 1,000 nm - mean 350 nm; Fig. 2c). Pol-spt show an enrichment in Cr (mean 1.18±0.89 wt.%) and to a lesser extent in Al (mean 4.32±2.53 wt.%) and Fe (mean 4.96±0.91 wt.%,) in comparison with the high temperature serpentines (i.e., the bastite, the mesh serpentine and the serpentine contouring spinels) (Fig. 3, Supplementary Fig. 2 and

Supplementary Table 1). Conversely, the pol-spt display low concentrations in cobalt (0.07±0.12 wt.%) and manganese (0.06±0.08 wt.%) while nickel reaches concentrations similar to what was found for the four other types of serpentine (0.22±0.25 wt.%). When numerous, pol-spt appear to fracture the H-adr crystals (Fig. 2b). This peculiar type of serpentine is also visible around the hydrogarnets, filling various-sized voids around the H-adr spheroids (Figs. 2a, c and e), with a clear indentation of the spheroids within the surrounding fine-grained bastite (Fig. 2f). H-adr crystals and part of the bastite were progressively replaced by pol-spt that also spread inside the surrounding remaining bastite through tiny veins (Figs. 2g-h).

The identification of pol-spt serpentines was confirmed by TEM and SAED (Figs. 4 and 5d). As described in literature (Baronnet and Devouard, 1996, 2005; Baronnet et al., 2007; Andreani et al., 2008; Cressey et al., 2008, 2010), polyhedral serpentine is composed of triangular facets made of lizardite basal planes showing lateral continuity from one sector to another and forming tiny "onion like" geodesic spheroids (Fig. 4). The core of the spheroids usually hosts a small fibre contoured by the triangular facets. Given that the geodesic spheroids have the simplest formulation as icosahedra, the inner cavity is possibly defined by this geometric limit. Polygonal serpentine crystallizes as tiny fibres composed of concentric lizardite layers wrapped around the fibre axis and made of 15 or 30 sectors (Fig. 5d). The fifteen-sector fibres are the smallest (< 400 nm - mean 350 nm), whereas the thirty-sector ones are larger (up to 1,000 nm - mean 610 nm).

SEM and TEM analyses highlight a close connection between pol-spt and H-adr (Figs. 5a-b). The globular topography of the H-adr inner cavities where pol-spt grew suggests local transformation of H-adr into spherical and coalescent pol-spt (Fig. 5a). TEM analyses of FIB foils milled on H-adr grains also show that the pol-spt enclosed in the branched and elongated dissolution cavities are embedded in a carbon-rich phase also covering the H-adr walls (Figs. 5b, d-g). This is in agreement with SEM observations collected on resin-free chips showing the presence of carbon veils within the H-adr cavities (Fig. 5c). The organic film has a gel-like appearance and does not show any structure or atomic organization using HR-TEM. It presents very low wetting angles with respect to the phyllosilicate and the hydrogarnet (Figs. 5b and d). TEM-EDXS analyses

highlight the presence of Mg, Si and to a lesser extent, Ca and Fe in the gel (Fig. 5e), likely responsible for the brightness of the fluffy phase observed by HAADF-STEM (Figs. 5f-g). The organic nature of the carbon gel was further demonstrated by STXM coupled with C-XANES spectroscopy. As displayed in Fig. 6e, the C-XANES spectrum of the carbon gel shows a major peak at 288.6 eV, characteristic of carboxylic functional groups (Cody et al., 1998; Benzerara et al., 2004; Bernard et al., 2009). STXM mapping shows that this organic phase is spectroscopically homogeneous (Figs. 6d-e).

3.2. Local enrichments in transition metals and associated carbon speciation

Carbon-rich areas are also found as large patches in H-adr inner cracks and fractures nearby iron oxides which precipitated concomitantly with H-adr (Fig. 7a). These carbon-rich patches are associated with a complex intergrowth of late stage serpentines including pol-spt among numerous nanometric to micrometric fibrous chrysotile-like aggregates (Figs. 7 and 8a). These felt-like organic matter accumulations are associated with enrichments in transition metals, notably cobalt (Fig. 8c; Ménez et al., 2012) but also manganese (Fig. 8b) and to a lesser extent iron and nickel (Figs. 9e-h, 10 and 11). These metals are strictly confined to the H-adr filling material and not dispersed in the host groundmass although some metal-rich nanophases can also be suspected in the bastite and the mesh serpentine, based on EMPA (Supplementary Fig. 2 and Supplementary Table 1). With the exception of Fe, none of those elements were detected in the carbon gel embedding the pol-spt previously described in the branched and elongated dissolution cavities (Figs. 5 and 6).

The felt presents an organic C-rich component with variable texture and porosity, finely intermingled with various amounts of micro- to nano-crystallites. As an illustration, Fig. 9d (or Supplementary Fig. 3 for an enlarged version of Fig. 9d) shows that polyhedral serpentine geodesic spheroids and polygonal serpentines are embedded in a foamy carbon gel presenting a vesicular texture with gradients in the size of the vesicles. The foamy appearance can be a primary character or alternatively can have been induced by degassing of a light fraction or by cavitation under

vacuum during measurements. The significant decompression experienced during the recovery from the seafloor can also be invoked. Variations of the texture seem however to be correlated with the presence/absence of transition metals, the gel texture being locally more massive when the carbon and metal contents are respectively lower and higher (Fig. 9). The foamy C-bearing gel is associated with the presence of Co and minor Mn, Ni, and Fe (Figs. 9d, g and 11). In contrast, Fig. 9b shows a dense carbon-bearing phase spotted by subnanometric electron-dense phases that were identified as well-crystallized Co-oxides (Figs. 10a-b and 11), likely responsible for the enrichment in Co shown in Fig. 8c. In this area, Mn, Ni and Fe are also present in the C-phase but at lower concentrations (Figs. 9e-f and 11). Similarly, a compact carbon-poor and likely more crystalline matrix displaying high Mn concentrations was identified in the upper part of Fig. 9d (Supplementary Fig. 3), based on STEM-EDXS mapping (Fig. 9h). In this area, pol-spt spheroids are locally surrounded by well-crystallized Mn/Fe crusts measuring about 50 nm in thickness (Figs. 10c-d and 11). The surrounding C-bearing matrix also presents high Mn, and to a lesser extent Fe, Co and Ni concentrations (Figs. 9h and 10e-h). This is confirmed by the relatively high brightness of the corresponding area by HAADF-STEM (Fig. 9h). In some locations, abundant nanometer-sized rods of Fe-(oxyhydr)oxides were also found among the tiny fibres of magnesium silicates within the carbon gel (e.g., Fig. 9g). Overall, transition metals appear to be associated with the carbon-bearing phase but selectively enriched in two domains characterized by high and low carbon concentrations for the Co-rich and Mn-Fe(-Ni) enriched areas, respectively.

Energy-filtered STXM images and associated C-XANES spectra collected in the same areas show that these chemically-heterogeneous organic carbon micro-domains display distinguishable signatures (Fig. 12). Similarly to what has been found for the carbon gel embedding pol-spt in the branched and elongated dissolution cavities (Fig. 6), the Mn-enriched regions display mainly absorption features of carboxylic functional groups at 288.6 eV along with the presence at a lower amount of aliphatic carbon at 287.7 eV (Cody et al., 1998; Benzerara et al., 2004; Bernard et al., 2009). A peak at 290.4 eV was also observed. According to Chan et al. (2009), it can be indicative of carboxyl groups binding iron and possibly other metals. Compared to the Mn-enriched area, the

Co-rich foamy region shows increased and decreased levels in aliphatics and carboxyl functional groups, respectively, plus minor aromatic or olefinic carbon at 285.1 eV.

4. Discussion and implications

As hypothesized by Ménez et al. (2012), textural relationships provide evidence that both H-adr dissolution and bastite resorption came along with the crystallization of polygonal and polyhedral serpentine around the andraditic hydrogarnets and within their dissolution cavities (Figs. 2 and 5a-b). The pol-spt genetic link with Cr-rich hydrogarnets is also supported by EMPA showing enrichment of the pol-spt in Cr and to a lesser extent in Al and Fe in comparison with the high-temperatures serpentines (Fig. 3 and Supplementary Fig. 2). These elements could have been inherited from both the parent H-adr and the bastite, this latter being likely the source of Mg for the precipitation of pol-spt (Supplementary Fig. 2).

Dissolution has selectively affected the crystal cores and progressed radially toward the grain rims (e.g., Figs. 5c and 7c and Supplementary Fig. 1). This process led to the formation of large inner cavities interpreted by Ménez et al. (2012) as the result of a cryptoendolithic microbial activity. Note that the origin of the organics found in these rocks is not discussed in the present paper and readers are referred to Ménez et al. (2012) and Pasini et al. (2013) and to the extensive discussions on organics' systematics that can be found within. Dissolution cavities provided the open space required for polyhedral serpentine to form (Andreani et al., 2008), along with the appropriate temperature conditions. Indeed, while the mesh serpentine, the bastite, and the serpentine contouring spinels are representative of the static replacement of the high temperature paragenesis during the first stages of serpentinization (> 200°C; Klein et al., 2014), the pol-spt are instead representative of crystallization occurring after complete hydration of the host pyroxene. Moreover, as discussed by Ménez et al. (2012), their precipitation after H-adr, which forms below 200°C (Frost and Beard, 2007; Plümper et al., 2014) attests for low-temperature conditions in agreement with Andreani et al. (2008). These authors also suggest a general enrichment in trivalent

cations as a stabilizing factor for pol-spt nucleation. This requirement is met here when considering the aluminum and chromium concentrations in pol-spt, as measured by EMPA (Supplementary Fig. 2 and Supplementary Table 1). For iron, while pol-spt display with the vein spt the highest concentrations, we did not succeed in determining the ferric iron content of pol-spt based on EMPA (Pasini, 2013). Nonetheless, as H-adr iron is solely in the form of Fe(III), it may suggest that at least a fraction of the pol-spt iron is present as Fe(III).

In our study, we observe that polyhedral and polygonal serpentines crystallized together in spatially-restricted areas, hence suggesting that they likely derive from the same process. Polygonal serpentine has been viewed by some authors as a more stable phase compared to chrysotile, or alternatively, as an analogous of the polyhedral serpentine (Cressey et al., 2008, 2010). Accordingly, polygonal and polyhedral serpentines may both form from a similar precursor through different growth mechanisms. Based on textural and microstructural criteria, Andreani et al. (2008) suggest that polyhedral serpentines, which are always the last serpentine type to crystallize, directly nucleate and grow radially with a layer-by-layer mechanism from a proto-serpentine colloidal phase containing a continuous solid skeleton of polymers or aggregates bathed in a liquid phase. Whether the proto-serpentine gel includes organic carbon compounds either of biogenic or abiotic origin has up to now never been documented. In the present study, the strict association of pol-spt serpentines with a Mg- and Si-bearing organic phase embedding all spheroid and tubular structures and coating the hydrogarnets walls (Figs. 5-7) suggests that organic carbon plays a role in the formation and stabilization of polyhedral serpentine and may constitute a key component of this proto-serpentine phase described by Andreani et al. (2008) as mediating the formation of polyhedral serpentines. This is supported by the presence of Mg-rich C-inclusions hosted in well-crystallized serpentine in the vicinity of the carbon gel (Figs. 9b and e) suggesting that organic carbon was involved in the last serpentinization events affecting the rock and not lately added to the system.

Further investigations are nonetheless needed to confirm the systematic presence of organic carbon associated with the formation of polyhedral serpentine in various settings. If true, polyhedral serpentines as a common mineral of the serpentinized oceanic lithosphere (e.g., Andreani et al.,

2007; Baronnet et al., 2007: Rouméjon et al., 2015) may then be used as a proxy for the presence of organic carbon within serpentinites. The presence of cronstedtite-derived polyhedral serpentine reported in carbonaceous chondrites (Zega et al., 2006) may also support this idea. Carbonaceous chondrites are known to contain a rich mixture of complex organic compounds (e.g., Schmitt-Kopplin et al., 2010). As shown by Elmaleh et al. (2015), the complex oxidation mechanisms of Fe-rich serpentines close to the cronstedtite endmember, which are abundant alteration products in chondrites, promote molecular hydrogen production and hence potential pathways for inorganic carbon reduction. If organic carbon is mandatory for pol-spt to form, then it would provide constrains on the timing of abiotic organic synthesis during the aqueous alteration of carbonaceous chondrites, the polyhedral serpentine being already considered as the endmember of an intense alteration sequence which may have occurred early in the chondrite or parent body history (Browning et al., 1996; Zega et al., 2006).

From another perspective, understanding how to promote the formation of pol-spt may have additional implications, notably for subsurface CO_2 storage. Due to the chemical potential of serpentinization to favor carbonation (i.e., CO_2 conversion into solid carbonates), ultramafic rocks have long been proposed as potential hosts for long lasting and safe storage of anthropogenic CO_2 in the attempt to stem the currently observed consequences on climate change and ocean acidification (e.g., Matter and Kelemen, 2009). One of the major criticisms raised against such a technology is the high clogging potential of lizardite which subsequently forms in veins and fractures following fluid-rock interactions and is commonly found as extremely fine-grained scales and massive aggregates (e.g., Farough et al., 2016). If organics, by controlling the size and shape of low-temperature serpentine types, promote instead the formation of pol-spt spheroids or tiny tubules in veins and fractures, as observed in Figs. 2g-h, fluid flow would then be improved together with the hydrodynamic properties of serpentinite.

Although the scattering of the data is large due to the small size of the spheroids and rods compared to the electron beam size, EPMA suggest that pol-spt have incorporated a limited amount of divalent metals in their structure (Fig. 3, Supplementary Fig. 2 and Supplementary Table 1).

Indeed, pol-spt display low concentrations in cobalt and manganese while nickel reaches higher concentrations (Supplementary Fig. 2 and Supplementary Table 1). Then, instead of being mobilized by aqueous fluids during hydrothermal alteration, as generally acknowledged during serpentinization (Pinto et al., 20017), metals unaccommodated by the pol-spt are found in the surrounding carbon gel where their speciation and mobility are apparently dictated by the concentration and the type of associated organic compounds (Fig. 12). The latter can be variable at the microscale, as attested by the chemically-heterogeneous organic carbon micro-domains highlighted by STEM-EDXS (Figs. 9 and 11) and STXM (Fig. 12). Cobalt is systematically associated with carbon, sometimes in the form of well-crystallized Co-oxides accompanied by lower concentrations of Mn, Ni, and Fe (Figs. 9e-h, 10a-b and 11). Mn-oxides are found in carbon-poor areas also enriched in Fe and Ni, forming nanometric crusts around pol-spt spheroids (Figs. 9h, 10c-h and 11).

Different processes can account for the local formation of these metallic oxides. Both Co and Mn in their divalent form are soluble ions in hydrothermal fluids and the presence of metallic oxides strongly suggests that oxidation, at least partial, occurred, turning Co(II) and Mn(II) into insoluble Co(III) and Mn(III) or Mn(IV), and leading to the precipitation of Co- and Mn-oxides. Whereas in the open ocean, organic-metal complexation reduces metal reactivity, increases their solubility and limits their scavenging into or onto particulate phases (Bennett et al., 2008), the presence of organic compounds in the present system did not play the same protective role as oxidation could have been responsible for the immobilization of metals. Although oxidative dissolution, as observed in the case of hydrothermal sulfides (German et al., 1991), cannot be totally excluded, Co and Mn oxidation is a process primarily known to be mediated by bacteria (Murray et al., 2007), in agreement with Ménez et al. (2012) who hypothesized that biological activity could have been responsible for H-adr dissolution. Mn(II) oxidation can occur by direct enzymatic activity (e.g., Tebo et al., 2004) or by exposure to reactive oxygen species produced by cells (Learman et al., 2011). Mn(II) biological oxidation was demonstrated to represent an important process in the formation of ferromanganese nodules and crusts (Nealson, 2006), sometimes also

enriched in Co(III) (Lee and Tebo, 1994). In aquatic environments, microbial Co and Mn oxidation were also shown to be linked but the oxidation of Co can also possibly be related to the high oxidative capabilities of poorly-crystalline Mn-oxides (Liao et al. 2011; Murray et al., 2007). These latter are indeed known to strongly control the transfer of metals in polluted systems (Borch et al., 2010; Tebo et al., 2004). Due to their high sorptive capacities, Mn-oxides can also adsorb or incorporate substantial amount of metals such as Co, Ni and Fe (Nealson, 2006), as observed here (Figs 10 and 11). Accordingly, in our samples, they likely contributed to the enrichment in metals of the organic C-bearing phases.

The local enrichments in transition metals and the nucleation of nanocrystallites may also have been driven differentially by the organic matrix itself, depending on the affinity of metals with the reactive organic functional groups locally present. Based on what was postulated by Ménez et al. (2012), the organic compounds found in these rocks may have derived from the presence of former cryptoendolithic microbial ecosystems solubilizing substrates by structuring themselves in the form of biofilm. Biofilm are described as gel-like structures composed of cells and EPS showing high reactive site densities (Ha et al., 2010). Metallic divalent cations, leached from H-adr, bastite and inherited Fe-ox, may then have been differentially trapped by the negatively-charged functional groups present in EPS. By imposing diffusion-limited processes, low permeability EPS, well acknowledged to strongly impact metal dynamics (e.g., Templeton et al., 2001; Wang et al., 2016; Warren and Haack, 2001), may also have contributed to accumulate Co and Mn in spatially-restricted areas, hence leading to the precipitation of metallic oxides once the supersaturation with respect to these oxides was locally reached. STXM imaging highlights that local enrichments in transition metals are selectively associated with different types and concentrations of organic carbon (Fig. 12). Cobalt was found within a carbon-rich gel-like mixture containing higher amount of aliphatics and lower amount of carboxylic compounds in comparison with the Mn-enriched C-poor micro-domain. However, the higher abundance of carboxyl groups in the Mn-enriched area suggests that, in this micro-domain, organic compounds may have been oxidized by the Mn-oxides, hence exerting locally a control on the redox state of the system. Note in addition that Co-oxides are

known catalysts for abiotic organic synthesis down to 30°C (e.g., Melaet et al., 2014; Varma et al., 2018). In this respect, once accumulated in the organic matrix, they also likely impacted the evolution of these organic molecules. However, the STXM spectrum of the Mn/Fe-bearing felt presents similarities with the one obtained in the carbon gel embedding pol-spt in the H-adr cavities (Fig. 6) and for which no enrichment in transition metals was shown. It will hence deserve further investigations notably on metal speciation.

Overall, whatever the detailed mechanisms involved, our observations demonstrate that organic compounds have the potential to immobilize metals in the form of metallic oxides or as metal ions adsorbed onto organic matrices during low-temperature hydrothermal alteration of the mantle-derived crust. If the impact of such processes on metal cycles is difficult to assess at the scale of the oceanic lithosphere in the present state of knowledge, it may have implications for ophiolites where active serpentinization also occurs. Ophiolitic massifs experiencing supergene alteration are the target for ore exploration and mining. Notably, tropical alteration of ophiolites yields lateritic cap rocks locally enriched in Co and Mn (Butt and Cluzel, 2013). As an illustration, Dublet et al. (2017) recently described the vertical changes in Co and Mn speciation along a lateritic regolith developed as a function of weathering stage upon peridotites from New Caledonia where mining activities exploit nickel-bearing ore over 6 000 km^2. They raised the question of the role of Mn- vs. Fe-(oxyhydr)oxides on Co speciation and on the long-term stabilization of metals at the whole regolith scale. Considering that the ophiolitic massif might host active microbial communities over a large depth, as it was recently demonstrated in Oman (Miller et al., 2016; Rempfert et al. 2017), we suggest that organic compounds along with microbial activities should also be investigated in the regolith and its underlying basement to assess their respective impact on Mn and Co speciation (± Ni and Fe) and hence on supergene ore formation, as already highlighted for gold or platinum-group elements (Reith et al., 2010, 2016).

5. Conclusions

We show in this study that high resolution spectroscopy and microscopy are a powerful approach to image organic compounds trapped in the porosity of serpentinites and to investigate their co-occurrences with metals and minerals. We strongly suggest that organic compounds, whose origin can be diverse in serpentinites (both abiotic and biogenic), locally influence low temperature (< 200°C) fluid-rock interactions in the serpentinizing oceanic lithosphere with consequences on metal distribution, speciation and hence mobility, as well as on the nature and structure of late stage mineralizations such as polygonal and polyhedral serpentines. Given the growing body of evidences showing that the serpentinized oceanic lithosphere constitutes a large habitat for life and that serpentinization reactions have a high potential for abiotic organic synthesis, it is then reasonable to expect such processes to be widespread in ultramafic rocks.

Acknowledgements

The authors are grateful to A. Cipriani (Univ. Modena e Reggio Emilia) who made available the sample collection recovered during the S22 expedition. We thank A. Gualtieri for his TEM expertise on serpentine, O. Boudouma for the assistance during SEM, D. Troadec for milling the FIB ultrathin section, and Javier Escartin for the bathymetric map of the Sierra Leone Fracture Zone. B.M. thanks Alexandre Gélabert and Thaïs Couasnon for stimulating discussion along with Jeff Alt and one other anonymous reviewer for constructive reviews. This work was supported by the French National Research Agency ANR through the deepOASES project granted to B.M. [grant number ANR-14-CE01-0008], Fondazione Cassa di Risparmio di Modena through the CARBRIDGE project (granted to D.B.), and an ECORD Research Grant 2010 to V.P. Support of the Deep Energy Community from the Deep Carbon Observatory awarded by Alfred P. Sloan Foundation is also acknowledged. STXM data were acquired at ALS beamline 5.3.2.2, which is supported by the Director of the Office of Science, Department of Energy [contract number DE-AC02-05CH11231]. Special thanks go to D. Kilcoyne for his expert support. The TEM facility at IMPMC was purchased owing to a support by Region Ile-de-France grant SESAME 2000 E 1435.

This is IPGP contribution n° XXXXX.

References

Andreani, M., Mével, C., Boullier, A.M., Escartín, J., 2007. Dynamic control on serpentine crystallization in veins: constraints on hydration processes in oceanic peridotites. Geochemistry Geophysics Geosystems 8, Q02012.

Andreani, M., Grauby, O., Baronnet, A., Munoz, M., 2008. Occurrence, composition and growth of polyhedral serpentine. European Journal of Mineralogy 20, 159-171.

Baronnet, A., Devouard, B., 1996. Topology and crystal growth of natural chrysotile and polygonal serpentine. Journal of Crystal Growth 166, 952-960.

Baronnet, A., Devouard, B., 2005. Microstructures of common polygonal serpentines from axial HRTEM imaging, electron diffraction, and lattice simulation data. The Canadian Mineralogist 43, 513-542.

Baronnet, A., Andreani, M., Grauby, O., Devouard, B., Nitsche, S., Chaudanson, D., 2007. Onion morphology and microstructure of polyhedral serpentine. American Mineralogist 92, 687-690.

Bassim, B.T., Kilcoyne, A.L.D., Scott, K., Chou, T., Wirick, S., Cody, G., Stroud, R.M., 2012. Minimizing damage during FIB sample preparation of soft materials. Journal of Microscopy 245, 288-301.

Bennett, S.A., Achterberg, E.P., Connelly, D.P., Statharn, P.J., Fones, G.R., Gernian, C.R., 2008. The distribution and stabilisation of dissolved Fe in deep-sea hydrothermal plumes. Earth and Planetary Science Letters 270, 157-167.

Bennett, S.A., Statham, P.J., Green, D.R.H., Le Bris, N., McDermott, J.M., Prado, F., Rouxel, O.J., Von Damm, K., German, C.R., 2011. Dissolved and particulate organic carbon in hydrothermal plumes from the East Pacific Rise, 9°50'N. Deep Sea Research Part I 58, 922-931.

Benzerara, K., Yoon, T.H., Tyliszczak, T., Constantz, B., Spormann, A.M., Brown Jr., G.E., 2004. Scanning transmission X-ray microscopy study of microbial calcification. Geobiology 2, 249-259.

Benzerara, K., Menguy, N., Guyot, F., Vanni, C., Gillet, P., 2005. High resolution study of silicate-

carbonate-micro-organism interface prepared by focused ion beam (FIB). Geochimica et Cosmochimica Acta 69, 1413-1422.

Bernard, S., Benzerara, K., Beyssac, O., Brown Jr., G.E., Stamm, L.G., Duringer, P., 2009. Ultrastructural and chemical study of modern and fossil sporoderms by Scanning Transmission X-ray Microscopy (STXM). Review of Palaeobotany and Palynology 156, 248-261.

Borch, T., Kretzschmar, R., Kappler, A., Van Cappellen, P., Ginder-Vogel, M., Voegelin, A., Campbell, K., 2010. Biogeochemical redox processes and their impact on contaminant dynamics. Environmental Science & Technology 44, 15-23.

Boyd, P.W., Ellwood, M.J., 2010. The biogeochemical cycle of iron in the ocean. Nature Geoscience 3, 675-682.

Browning, L.B., McSween, H.Y. Jr., Zolensky, M.E., 1996. Correlated alteration effects in CM carbonaceous chondrites. Geochimica et Cosmochimica Acta 60, 2621-2633.

Butt, C.R., Cluzel, D., 2013. Nickel laterite ore deposits: weathered serpentinite. Elements 9, 123-128.

Chan, C.S., Fakra, S.C., Edwards, D.C., Emerson, D., Banfield, J.F., 2009. Iron oxyhydroxide mineralization on microbial extracellular polysaccharides. Geochimica et Cosmochimica Acta 73, 3807-3818.

Cody, G.D., Ade, H., Wirick, S., Mitchell, G.D., Davis, A., 1998. Determination of chemical-structural changes in vitrinite accompanying luminescence alteration using C-NEXAFS analysis. Organic Geochemistry 28, 441-455.

Cressey, G., Cressey, B.A., Wicks, F.J., 2008. Polyhedral serpentine: a spherical analogue of polygonal serpentine? Mineralogical Magazine 72, 1229-1242.

Cressey, G., Cressey, B.A., Wicks, F.J., Yada, K., 2010. A disc with fivefold symmetry: the proposed fundamental seed structure for the formation of chrysotile asbestos fibres, polygonal serpentine fibres and polyhedral lizardite spheres. Mineralogical Magazine 74, 29-37.

Dublet, G., Juillot, F., Brest, J., Noël, V., Fritsch, E., Proux, O., Olivi, L., Ploquin, F., Morin, G.,

2017. Vertical changes of the Co and Mn speciation along a lateritic regolith developed on peridotites (New Caledonia). Geochimica et Cosmochimica Acta 217, 1-15.

Elmaleh, A., Bourdelle, F., Caste, F., Benzerara, K., Leroux, H., Devouard, B., 2015. Formation and transformations of Fe-rich serpentines by aqueous alteration in asteroids: a nanoscale study of the Murray chondrite. Geochimica et Cosmochimica Acta 158, 162-178.

Farough, A., Moore, D.E., Lockner, D.A., Lowell, R.P., 2016. Evolution of fracture permeability of ultramafic rocks undergoing serpentinization at hydrothermal conditions: An experimental study. Geochemistry, Geophysics, Geosystems 17, 44-55.

Field, M.P., Sherrell, R.M., 2000. Dissolved and particulate Fe in a hydrothermal plume at 9°45′N, East Pacific Rise: Slow Fe(II) oxidation kinetics in Pacific plumes. Geochimica et Cosmochimica Acta 64, 619-628.

Fitzsimmons, J.N., John, S.G., Marsay, C.M., Hoffman, C.L., Nicholas, S.L., Toner, B.M., German, C.R., Sherrell, R.M., 2017. Iron persistence in a distal hydrothermal plume supported by dissolved–particulate exchange. Nature Geoscience 10, 195-201.

Frost, B.R., Beard, J.S., 2007. On silica activity and serpentinization. Journal of Petrology 48, 1351–1368.

German, C.R., Campbell, A.C., Edmond, J.M., 1991. Hydrothermal scavenging at the Mid-Atlantic Ridge: modification of trace element dissolved fluxes. Earth and Planetary Science Letters 107, 101-114.

Ha, J., Gélabert, A., Spormann, A.M., Brown, G.E., Jr., 2010. Role of extracellular polymeric substances in metal ion complexation on *Shewanella oneidensis*: Batch uptake, thermodynamic modeling, ATR-FTIR, and EXAFS study. Geochimica et Cosmochimica Acta 74, 1-15.

Hawkes, J.A., Connelly, D.P., Gledhill, M., Achterberg, E.P., 2013. The stabilization and transportation of dissolved iron from high temperature hydrothermal vent systems. Earth and Planetary Science Letters 375, 280-290.

Hawkes, J.A., Rossel, P.E., Stubbins, A., Butterfield, D., Connelly, D.P., Achterberg, E.P.,

Koschinsky, A., Chavagnac, V., Hansen, C.T., Bach, W., Dittmar, T., 2015. Efficient removal of recalcitrant deep-ocean dissolved organic matter during hydrothermal circulation. Nature Geoscience 8, 856-860.

Kawka, O.E., Simoneit, B.R.T., 1987. Survey of hydrothermally-generated petroleums from the Guaymas Basin spreading center. Organic Geochemistry 11, 311-328.

Klein, F., Bach, W., Humphris, S.E., Kahl, W.-A., Jöns, N., Moskowitz, B., Berquó, T.S., 2014. Magnetite in seafloor serpentinite-Some like it hot. Geology 42, 135-138.

Klevenz, V., Bach, W., Schmidt, K., Hentscher, M., Koschinsky, A., Petersen, S., 2011. Geochemistry of vent fluid particles formed during initial hydrothermal fluid-seawater mixing along the Mid-Atlantic Ridge. Geochemistry, Geophysics Geosystems 12 (10), Q0AE05.

Kilcoyne, A.L., Tyliszczak, T., Steele, W.F., Fakra, S., Hitchcock, P., Franck, K., Anderson, E., Harteneck, B., Rightor, E.G., Mitchell, G.E., Hitchcock, A.P., Yang, L., Warwick, T., Ade, H., 2003. Interferometer-controlled scanning transmission X-ray microscopes at the Advanced Light Source. Journal of Synchrotron Radiation 10, 125–136.

Konn, C., Charlou, J.L., Holm, N.G., Mousis, O., 2015. The production of methane, hydrogen, and organic compounds in ultramafic-hosted hydrothermal vents of the Mid-Atlantic Ridge. Astrobiology 15, 381-399.

Lang, S.Q., Butterfield, D.A., Lilley, M.D., Paul Johnson, H., Hedges, J.I., 2006. Dissolved organic carbon in ridge-axis and ridge-flank hydrothermal systems. Geochimica et Cosmochimica Acta 70, 3830-3842.

Lau, B.L.T., Hsu-Kim H., 2008. Precipitation and growth of zinc sulfide nanoparticles in the presence of thiol-containing natural organic ligands. Environmental Science & Technology 42, 7236-7241.

Learman, D.R., Wankel, S.D., Webb, S.M., Martinez, N., Madden, A.S., Hansel, C.M., 2011. Coupled biotic-abiotic Mn(II) oxidation pathway mediates the formation and structural evolution of biogenic Mn oxides. Geochimica et Cosmochimica Acta 75, 6048-6063.

Lee, Y., Tebo, B.M., 1994. Cobalt(II) oxidation by the marine manganese(II)-oxidizing *Bacillus* sp.

strain SG-1. Applied and Environmental Microbiology 60, 2949-2957.

Lepot, K., Benzerara, K., Brown, G.E., Jr., Philippot P., 2009. Organic matter heterogeneity in 2.72 Ga stromatolites: alteration versus preservation by sulphur incorporation. Geochimica et Cosmochimica Acta 73, 6579-6599.

Liao, L., Xu, X.W., Jiang, X.W., Wang, C.S., Zhang, D.S., Ni, J.Y., Wu, M., 2011. Microbial diversity in deep-sea sediment from the cobalt-rich crust deposit region in the Pacific Ocean. FEMS Microbiology Ecology 78, 565-585.

Mason, O.U., Nakagawa, T., Rosner, M., Van Nostrand, J.D., Zhou, J., Maruyama, A., Fisk, M.R., Giovannoni, S.J., 2010. First investigation of the microbiology of the deepest layer of ocean crust. PLoS One 5:e15399.

Matter, J.M., Kelemen, P.B., 2009. Permanent storage of carbon dioxide in geological reservoirs by mineral carbonation. Nature Geoscience 2, 837-841.

Melaet, G., Ralston, W.T., Li, C.S., Alayoglu, S., An, K., Musselwhite, N., Kalkan, B., Somorjai, G.A., 2014. Evidence of highly active cobalt oxide catalyst for the Fischer-Tropsch synthesis and CO_2 hydrogenation. Journal of the American Chemical Society 136, 2260-2263.

Ménez, B., Pasini, V., Brunelli, D., 2012. Life in the hydrated suboceanic mantle. Nature Geoscience 5, 133-137.

Miller, H.M., Matter, J.M., Kelemen, P., Ellison, E.T., Conrad, M.E., Fierer, N., Ruchala, T., Tominaga, M., Templeton, A.S., 2016. Modern water/rock reactions in Oman hyperalkaline peridotite aquifers and implications for microbial habitability. Geochimica et Cosmochimica Acta 179, 217-241.

Monnin, C., Chavagnac, V., Boulart, C., Ménez, B., Gérard, M., Gérard, E., Pisapia, C., Quéméneur, M., Erauso, G., Postec, A., Guentas-Dombrowski, L., Payri, C., Pelletier, B., 2014. Fluid chemistry of the low temperature hyperalkaline hydrothermal system of Prony Bay (New Caledonia). Biogeosciences 11, 5697-5706.

Mottl, M.J., McConachy, T.F., 1990. Chemical processes in buoyant hydrothermal plumes on the East Pacific Rise near 21-degrees-N. Geochimica et Cosmochimica Acta 54, 1911-1927.

Murray, K.J., Webb, S.M., Bargar, J.R., Tebo, B.M., 2007. Indirect oxidation of Co(II) in the presence of the marine Mn(II)-oxidizing bacterium *Bacillus* sp strain SG-1. Applied and Environmental Microbiology 73, 6905-6909.

Nealson, K.H., 2006. The manganese-oxidizing bacteria. In: Prokaryotes (Dworkin, M., Falkow, S., Rosenberg, E., Schleifer, K.H., Stackebrandt, E., eds), Springer, New York, N.Y., vol. 5, 222-231.

Pasini, V., 2013. Biopetrology of the hydrating mantle along Mid-Ocean ridges. Ph.D manuscript. Università di Modena e Reggio Emilia & Institut de Physique du Globe de Paris, 308 p.

Pasini, V., Brunelli, D., Dumas, P., Sandt, C., Frederick, J., Benzerara, K., Bernard, S., Ménez, B., 2013. Low temperature hydrothermal oil and associated biological precursors in serpentinites from Mid-Ocean ridge. Lithos 178, 84-95.

Pinto, V.H.G., Manatschal, G., Karpoff, A.M., Ulrich, M., Viana, A.R., 2017. Seawater storage and element transfer associated with mantle serpentinization in magma-poor rifted margins: A quantitative approach. Earth and Planetary Science Letters 459, 227-237.

Plümper, O., Beinlich, A., Bach, W., Janots, E., Austrheim, H., 2014. Garnets within geode-like serpentinite veins: Implications for element transport, hydrogen production and life-supporting environment formation. Geochimica et Cosmochimica Acta 141, 454-471.

Peive, A.A., Savel'eva, G.N., Skolotnev, S.G., Simonov, V.A., 2003. Tectonics and origin of the oceanic crust in the region of 'dry' spreading in the Central Atlantic (7°10′5°N). Geotectonics 37, 3-25.

Reith, F., Fairbrother, L., Nolze, G., Wilhelmi, O., Clode, P.L., Gregg, A., Parsons, J.E., Wakelin, S.A., Pring, A., Hough, R., Southam, G., Brugger, J., 2010. Nanoparticle factories: biofilms hold the key to gold dispersion and nugget formation. Geology 38, 843-846.

Reith, F., Zammit, C.M., Saad Shar, S., Etschmann, B., Bottrill, R., Southam, G., Ta, C., Kilburn, M., Oberthür, T., Ball, A.S., Brugger, J., 2016. Biological role in the transformation of platinum-group mineral grains. Nature Geoscience 9, 294-298.

Rempfert, K.R., Miller, H.M., Bompard, N., Nothaft, D., Matter, J.M., Kelemen, P., Fierer, N.,

Templeton, A.S., 2017. Geological and geochemical controls on subsurface microbial life in the Samail ophiolite, Oman. Frontiers in Microbiology 8, 56.

Resing, J.A., Sedwick, P.N., German, C.R., Jenkins, W.J., Moffett, J.W., Sohst, B.M., Tagliabue, A., 2015. Basin-scale transport of hydrothermal dissolved metals across the South Pacific ocean. Nature 523, 200-203.

Rossel, P.E., Stubbins, A., Rebling, T., Koschinsky, A., Hawkes, J.A., Dittmar, T., 2017. Thermally altered marine dissolved organic matter in hydrothermal fluids. Organic Geochemistry 110, 73-86.

Rouméjon, S., Cannat, M., Agrinier, P., Godard, M., Andreani, M., 2015. Serpentinization and fluid pathways in tectonically exhumed peridotites from the southwest Indian ridge (62-65°E). Journal of Petrology 56, 703-734.

Sander, S.G., Koschinsky, A., 2011. Metal flux from hydrothermal vents increased by organic complexation. Nature Geoscience 4, 145-150.

Sander, S.G., Koschinsky, A., Massoth, G., Stott, M., Hunter, K.A., 2007. Organic complexation of copper in deep-sea hydrothermal vent systems. Environmental Chemistry 4, 81-89.

Sands, C.M., Connelly, D.P., Statham, P.J., German, C.R., 2012. Size fractionation of trace metals in the Edmond hydrothermal plume, Central Indian Ocean. Earth and Planetary Science Letters 319-320, 15-22.

Santelli, C.M., Orcutt, B.N., Banning, E., Bach, W., Moyer, C.L., Sogin, M.L., Staudigel, H., Edwards, K.J., 2008 Abundance and diversity of microbial life in ocean crust. Nature 453, 653-656.

Schmitt-Kopplin, P., Gabelica, Z., Gougeon, R.D., Fekete, A., Kanawati, B., Harir, M., Gebefuegi, I., Eckel, G., Hertkorn, N., 2010.High molecular diversity of extraterrestrial organic matter in Murchison meteorite revealed 40 years after its fall. Proceedings of the National Academy of Sciences of the United States of America 107, 2763-2768.

Schneider, C.A., Rasband, W.S., Eliceiri, K.W., 2012. NIH Image to ImageJ: 25 years of image analysis. Nature Methods 9, 671-675.

Schrenk, M.O., Brazelton, W.J., Lang, S.Q., 2013. Serpentinization, carbon and deep life. In: Hazen, R.M., Jones, A.P., Baross, J.A. (Eds.), Carbon in Earth. Reviews in Mineralogy and Geochemistry, 75. Mineralogical Society of America, Geochemical Society, pp. 575-606.

Seyfried, W.E., Jr., Pester, N.J., Tutolo, B.M., Ding, K., 2015. The Lost City hydrothermal system: Constraints imposed by vent fluid chemistry and reaction path models on subseafloor heat and mass transfer processes. Geochimica et Cosmochimica Acta 163, 59-79.

Sharkov, E., 2012. Cyclic development of axial parts of slow-spreading ridges: Evidence from Sierra Leone area, the Mid-Atlantic Ridge, 5-7°N. In: Sharkov, E. (Ed.), Tectonics - Recent Advances, pp. 3-36.

Simoneit, B.R.T., Lein, A.Y, Peresypkin, V.I., Osipov, G.A., 2004. Composition and origin of hydrothermal petroleum and associated lipids in the sulfide deposits of the Rainbow Field (Mid-Atlantic Ridge at 36°N). Geochimica et Cosmochimica Acta 68, 2275-2294.

Statham, P.J., German, C.R., Connelly, D.P., 2005. Iron(II) distribution and oxidation kinetics in hydrothermal plumes at the Kairei and Edmond vent sites, Indian Ocean. Earth and Planetary Science Letters 236, 588-596.

Tebo, B.M., Bargar, J.R., Clement, B.G., Dick, G.J., Murray, K.J., Parker, D., Verity, R., Webb, S.M., 2004. Biogenic manganese oxides: Properties and mechanisms of formation. Annual Review of Earth and Planetary Sciences 32, 287-328.

Templeton, A.S., Trainor, T.P., Traina, S.J., Spormann, A.M., Brown, G.E., 2001. Pb(II) distributions at biofilm-metal oxide interfaces. Proceedings of the National Academy of Sciences of the United States of America 98, 11897-11902.

Toner, B.M., Fakra, S.C., Manganini, S.J., Santelli, C.M., Marcus, M.A., Moffett, J.W., Rouxel, O., German, C.R., Edwards, K.J., 2009. Preservation of iron(II) by carbon-rich matrices in a hydrothermal plume. Nature Geoscience 2, 197-201.

Varma, S.J., Muchowska, K.B., Chatelain, P., Moran, J., 2018. Native iron reduces CO_2 to intermediates and end-products of the acetyl-CoA pathway. Nature Ecology & Evolution 2, 1019-1024.

Warren, L.A., Haack, E.A., 2001. Biogeochemical controls on metal behaviour in freshwater environments. Earth-Science Reviews 54, 261-320.

Wang, Y., Gélabert, A., Michel, F.M., Choi, Y., Gescher, J., Ona-Nguema, G., Eng, P.J., Bargar, J.R., Farges, F., Spormann, A.M., Brown, G.E., Jr, 2016. Effect of biofilm coatings at metal-oxide/water interfaces I: Pb(II) and Zn(II) partitioning and speciation at *Shewanella oneidensis*/metal-oxide/water interfaces. Geochimica et Cosmochimica Acta 188, 368-392.

Wu, J., Wells, M.L., Remember, R., 2011. Dissolved iron anomaly in the deep tropical–subtropical Pacific: Evidence for long-range transport of hydrothermal iron. Geochimica et Cosmochimica Acta 75, 460-468.

Zega, T.J., Garvie, L.A.J., Dódony, I., Friedrich, H., Stroud, R.M., Buseck, P.R., 2006. Polyhedral serpentine grains in CM chondrites. Meteoritic & Planetary Science 41, 681-688.

Figure captions

Fig. 1. (a) bathymetric map of the 0-10° N region showing within a white rectangle the location of the non-transform Sierra Leone Fracture Zone (FZ; 7°10′5 N) in the equatorial Mid-Atlantic Ridge where the sample S2232-17 has been dredged ("mbsl" stands for meters below sea level). (b) enlarged view of (a). (c) optical image of a cut section of the serpentinized S2232-17 rock; olivine was replaced by serpentine and magnetite exhibiting a characteristic mesh texture (mesh-spt); orthopyroxene was replaced by fine grained lizardite, defined as bastite (bast). Late veins of serpentine crosscut the whole (spt-vein). (d) photomicrograph in transmitted plane polarized light showing andraditic hydrogarnet (H-adr) ± iron oxides distributed along exsolution lamellae in the bastitized orthopyroxene. Clusters of hydrogarnets were also found close to the orthopyroxenes, filling veins and microfractures.

Fig. 2. SEM images of polygonal and polyhedral serpentine (pol-spt) rods and spherules of variable sizes (10-1,000 nm) found (a) surrounding a pierced andraditic hydrogarnet (H-adr), (b) filling in the interior of a fractured H-adr crystal enclosed in bastite (bast). (c) and (d) are enlarged views of a hydrogarnet selvage with (d) being located in (c) with a white rectangle. (e) and (f) show that the pol-spt coverage is uniform in the cavity where a hydrogarnet was formerly present. (f), which is a magnified view of (e) (location indicated by a white rectangle), shows indentation of the pol-spt within the fine grained orientated bastite. As hypothesized by Ménez et al. (2012), pol-spt are progressively replacing hydrogarnets in this rock with (g) illustrating an advanced dissolution stage with a hydrogarnet almost fully replaced by pol-spt. White arrows in (g) depict tiny veins (< 5 µm in width) of pol-spt branching out from the former H-adr location (detail shown in (h)). (a), (b) and (g) are reproduced from Ménez et al. (2012) with permission.

Fig. 3. Cr_2O_3 (wt.%) versus X_{Fe} diagram established from EMPA collected on the 5 groups of serpentines identified in the rock: the serpentine after olivine in the mesh texture (mesh spt), the

bastite after orthopyroxene (bast), the serpentine after olivine contouring spinels (spl spt), the polygonal and polyhedral serpentines associated with hydrogarnets (pol-spt) and the serpentine found in the late veins crosscutting the rock (vein spt) (Fig. 1c). The uncertainties associated to EMPA are within the symbol dimensions. X_{Fe} is defined as (total Fe)/(total Fe + Mg) and expresses the fraction of iron incorporated into serpentine. The enrichment in Cr and to a lesser extent in Fe and Al (see also Supplementary Fig. 2 and Supplementary Table 1) of the pol-spt, are in agreement with formation from hydrogarnet dissolution, the hydroandradite displaying mean formula of $Ca_{2.71}(Fe_{1.61}^{3+},Ti_{0.01},Al_{0.17},Cr_{0.03},Mg_{0.02})(Si_{2.92}O_{10.93})(OH)_{1.07}$.

Fig. 4. (a) TEM image collected on a FIB ultrathin section and showing a submicrometric spheroid grown in an elongated cavity inside a hydrogarnet (H-adr). The corresponding FIB section is shown in Fig. 6b. The spheroid was identified by SAED as geodesic polyhedral serpentine (pol-spt) whose model is drawn in the lower left inset in (b). The diffraction pattern is characteristic of a polycrystalline aggregate, with spots aligned along circles of increasing diameter due to the multiple orientations of each serpentine triangular facet. Measured inter-planar distances are compatible with lizardite lattice, in agreement with Andreani et al. (2008) who reported on the strict short-range similarity of the structure of polyhedral serpentine and lizardite, based on Raman spectroscopic characteristics.

Fig. 5. The nucleation and growth of polyhedral and polygonal serpentine (pol-spt) from the hydrogarnet (H-adr) dissolution appear to be mediated by a carbon-bearing gel-like phase. (a) SEM image of a H-adr cavity milled by FIB revealing enclosed pol-spt of variable size growing on a granular H-adr surface (see Supplementary Fig. 1 for SEM views of the corresponding H-adr and FIB foil). (b) TEM image detailing the pol-spt/H-adr interface. Submicrometric chrysotile fibres are also visible. The close connection between pol-spt and H-adr, highlighted at the location shown by the white asterisk, again suggests that pol-spt grew at the expense of hydrogarnets, hence confirming the genetic link between both. Moreover, it highlights continuous coating of the

assemblage by a gel-like phase (depicted by black arrows). The corresponding FIB section is shown in Fig. 7c. (c) magnified SEM view of H-adr dissolution cavities in which carbon veils can be found. (d) TEM image showing a 15 sector (upper fibre) and a 30 sector (bottom fibre) polygonal serpentine wet by a jelly film of carbon interfacing between the serpentine and the H-adr walls. The corresponding FIB section is shown in Fig. 6b. Star and diamond correspond to the locations of the EDXS spectra shown in (e) and collected on the carbon gel and the pol-spt, respectively. (e) associated EDXS spectra showing that the carbon gel is also bearing Si, Mg, and to a lesser extent, Ca and Fe, likely inherited from the hydrogarnet and the bastite. (f) HAADF-STEM image of a serpentine spheroid confirming the carbon gel to also bear heavier elements in addition to carbon. (g) associated STEM-EDXS elemental image showing the distribution of carbon (green).

Fig. 6. STXM characterization at the C K-edge of the carbon gel associated with polyhedral rods and polygonal serpentine spheroids (pol-spt) occurring in dissolution cavities of hydrogarnet (H-adr). (a) SEM image of a subhedral andraditic hydrogarnet showing pol-spt spreading. The location where the foil was milled is indicated by the orange dashed line. (b) SEM image of the FIB foil where dissolution pits and cavities filled with pol-spt spheroids are visible along with pol-spt covering the H-adr rim. The platinum coating aimed at protecting milled volumes before excavation. (c) TEM enlarged view of the area shown by a white square in (b) where pol-spt have crystallized in the H-adr dissolution cavity. White asterisk corresponds to the location of the pol-spt geodesic spheroid shown in Fig. 4. (d) composite STXM map showing the distribution of organic carbon (in red) in the mineral matrix (in green). The STXM image is located using a black square in (b). It confirms the organic nature of the carbon gel. (e) associated C-XANES spectrum showing mainly X-ray absorption of carboxyl functional groups at 288.6 eV.

Fig. 7. (a) SEM image in false colors of a mélange of polyhedral and polygonal serpentines (pol-spt in green), along with aggregated nanometric fibres forming a felt wet by a carbon-bearing matrix (yellow), all filling the cracks and voids of an andraditic hydrogarnet (H-adr in blue) hosting Fe-

oxides (orange). (b) SEM image of a H-adr where the FIB foil displayed in (c) was milled along the orange dashed line. It shows dissolution pits piercing its surface. SEM image of the FIB foil in (c) shows that these pits relate to deep inner and various-sized dissolution cavities enclosing large quantity of felt in H-adr. (d) associated TEM image showing pol-spt enclosed in aggregated tiny fibres likely responsible for the felt texture.

Fig. 8. (a) SEM image of a large accumulation of carbon-bearing felt embedding numerous polyhedral and polygonal serpentines (pol-spt) and trapped in a fractured hydrogarnet (H-adr) (modified from Ménez et al. (2012) with permission). The orange dashed lines show the locations where two FIB foils (shown in Fig. 9) were milled. (b) and (c): associated elemental distributions of magnesium (green), calcium (red), manganese (purple) and cobalt (blue). Mn and Co appear selectively enriched in two distinct regions of the carbon-rich felt filling H-adr cracks. (d) corresponding SEM-EDXS spectrum. Collection point is located by a white star in (c). Pt and Au arise from the metallic coating.

Fig. 9. Electron microscopy images of the metal-bearing felt collected on the FIB foil milled in the area enriched in Co [(a) and (b)] and on the FIB foil milled in the Mn-enriched region [(c) and (d)] and associated STEM characterizations [from (e) to (h)] (see Fig. 8a for milling locations). (a) SEM image of the FIB foil milled in the Co-enriched area. It shows a thin layer of felt interfacing an andraditic hydrogarnet (H-adr) and the FIB foil protective layer of platinum. (b) associated TEM images whose location is shown in (a). An enlarged view is shown is Fig. 10a. It shows black dots spotting the carbon gel enclosing polyhedral serpentine (pol-spt) and well-crystallized serpentine. (c) SEM image of the FIB foil milled in the Mn-enriched region showing felt enclosed within a fractured H-adr. (d) associated TEM images showing numerous pol-spt enclosed in a C-rich porous gel. An enlarged view is shown in Fig. 10c and in Supplementary Fig. 3. From (e) to (h): associated HAADF-STEM images and corresponding STEM-EDXS elemental distributions. Locations of (e)+(f) and (g)+(h) are shown using white squares in (b) and (c), respectively.

Fig. 10. Magnified TEM and STEM images of the metal-bearing felt collected on the FIB foil milled in the area enriched in Co [(a) and (b)] and on the FIB foil milled in the Mn-enriched region [from (c) to (h)] (Fig. 8a). Locations of (a) and (c) are indicated in Figs. 9b and 9d, respectively. (a) nanometric Co-oxides dispersed in the organic gel around a well-crystallized serpentine (spt) presenting non crystalline Mg- and C-bearing inclusion (Mg-C incl.). (b) associated HR-TEM image showing Co-oxides. (c) polyhedral serpentine (pol-spt) spheroid contoured by a crust of Mn and Fe close to an iron oxide (Fe-ox). (d) is a magnified view of (c) with location indicated by an orange star in (c). In (b) and (d), atom plane fringes attest for the presence of well-defined crystallographic planes (white arrows). (e) larger HAADF-STEM image of the encrusted pol-spt. Location of (c) is shown by a white square. From (f) to (h): STEM-EDXS elemental images showing the distribution of Fe (f), Mn (g) and Co (h). They show Co homogeneously distributed outside the pol-spt in both the C-bearing phase and the Fe-ox whereas Fe and, to a lesser extent, Mn are enriched in the metallic crust contouring some of the pol-spt. Associated STEM-EDXS spectra are shown in Fig. 11.

Fig. 11. TEM-EDXS spectra associated with (1) the polyhedral serpentine (pol-spt), (2) the Mn/Fe crust formed around the pol-spt shown in Figs. 10c-h, (3) the nanometric Co-oxides shown in Figs. 10a-b, (4) the carbon matrix found in the felt. Cu X-ray peak at 8 keV arises from the TEM grid.

Fig. 12. STXM characterization of the metal-bearing felt enclosed in a fractured hydrogarnet. Analysis have been performed on the FIB foil displayed in Fig. 9c with associated TEM and STEM-EDXS characterizations shown in Fig. 9d and Figs. 9g-h, respectively. (a) composite STXM map showing the distribution of the Co- and Mn/Fe-bearing organic components contained in the felt and appearing respectively in blue and green. The red colour figures the location of the silicate component. (b) composite STEM-EDXS elemental image showing the distribution of Mg (red), Mn

(green) and Co (blue) in the area indicated by a white square in (a), as also shown in Fig. 9h. (c) C-XANES spectra associated with the Co-bearing area and the Mn-enriched felt. It shows the presence of aromatic or olefinic carbon (285.1 eV), aliphatic carbon (287.7 eV), and carboxyl functional groups (288.6 eV). The peak at 290.4 eV can be related to carboxyl groups bounded to metals.

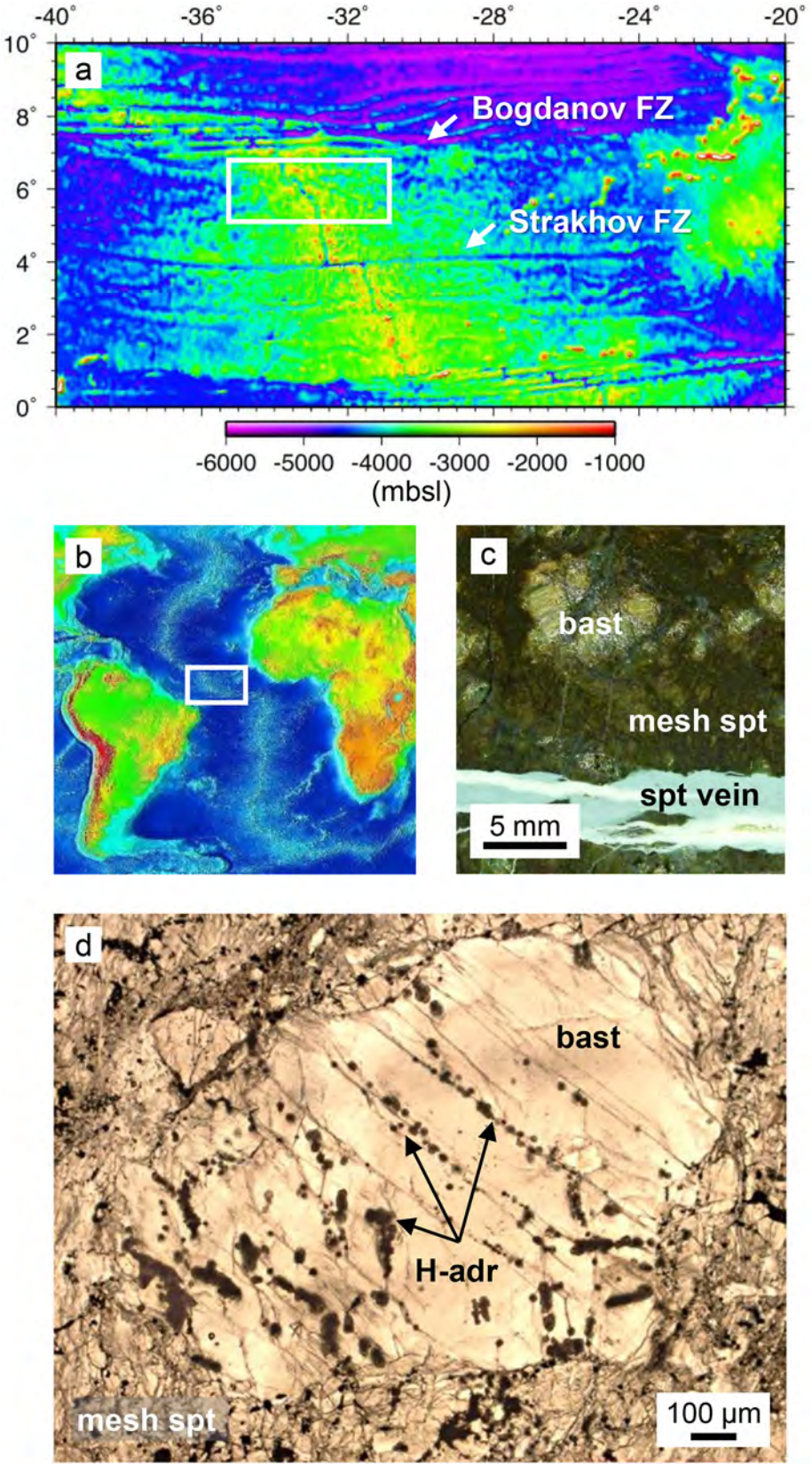
-40°
-36°
-32°
-28°
-24°
-20°
10°
8°
6°
4°
2°
0°
a
Bogdanov FZ
Strakhov FZ
-6000 -5000 -4000 -3000 -2000 -1000
(mbsl)
b
c
bast
mesh spt
spt vein
5 mm
d
bast
H-adr
mesh spt
100 µm

Figure 1

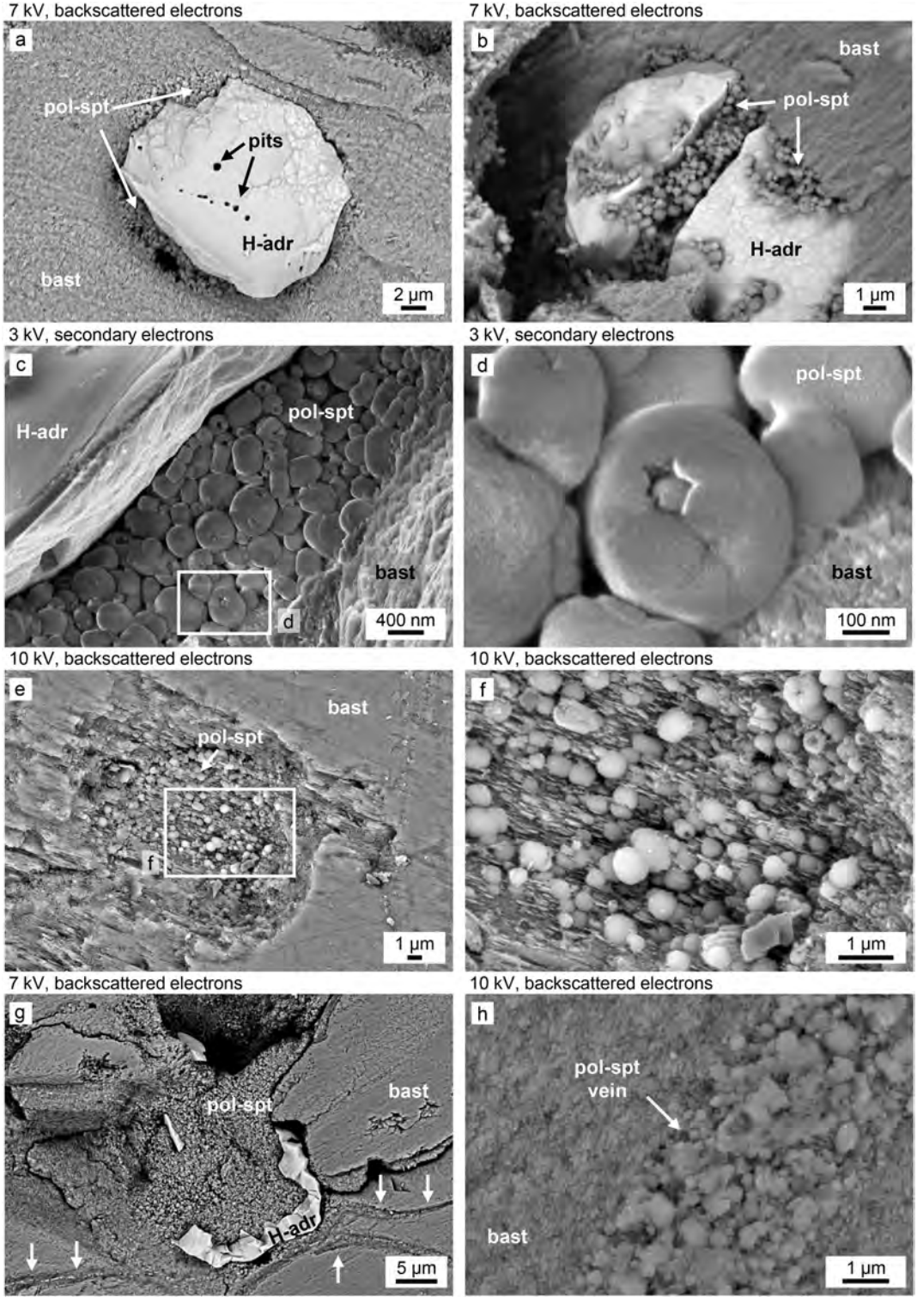
7 kV, backscattered electrons
a
pol-spt
pits
H-adr
bast
2 µm
7 kV, backscattered electrons
b
bast
pol-spt
H-adr
1 µm
3 kV, secondary electrons
c
H-adr
pol-spt
bast
d
400 nm
3 kV, secondary electrons
d
pol-spt
bast
100 nm
10 kV, backscattered electrons
e
bast
pol-spt
f
1 µm
10 kV, backscattered electrons
f
1 µm
7 kV, backscattered electrons
g
pol-spt
bast
H-adr
5 µm
10 kV, backscattered electrons
h
pol-spt
vein
bast
1 µm

Figure 2

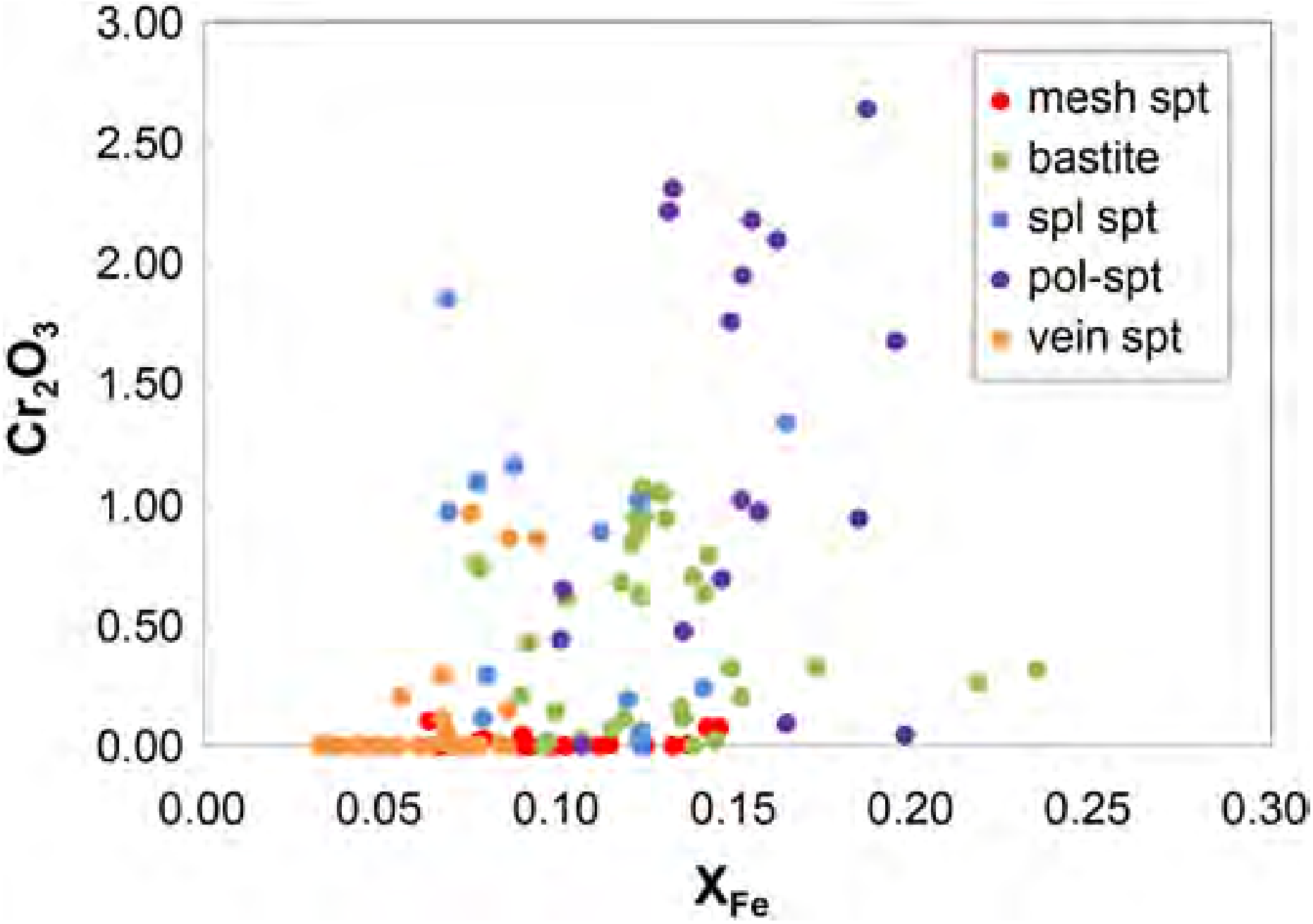
3.00
2.50
2.00
1.50
1.00
0.50
0.00
Cr_2O_3
0.00
0.05
0.10
0.15
0.20
0.25
0.30
X_{Fe}
mesh spt
bastite
spl spt
pol-spt
vein spt

Figure 3

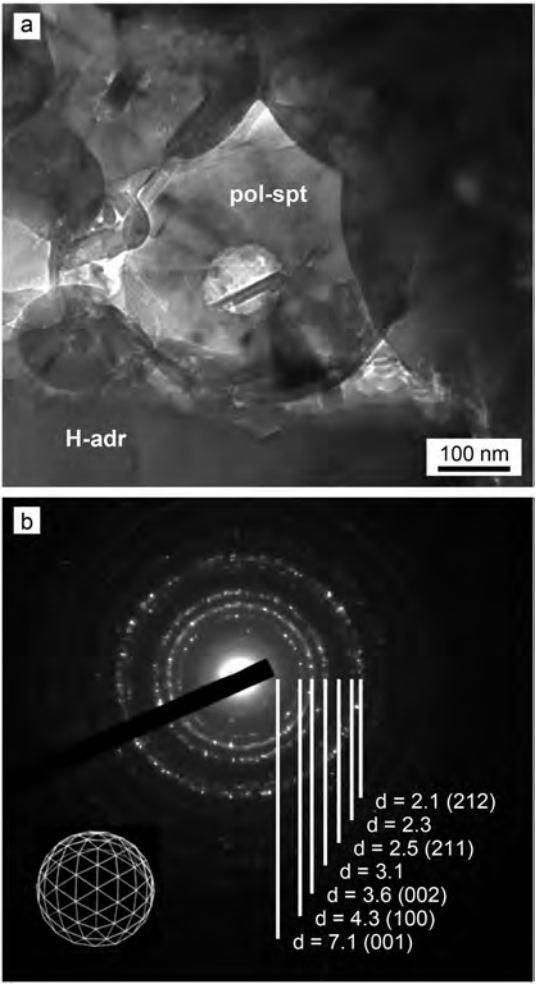
a
pol-spt
H-adr
100 nm
b
d = 2.1 (212)
d = 2.3
d = 2.5 (211)
d = 3.1
d = 3.6 (002)
d = 4.3 (100)
d = 7.1 (001)

Figure 4

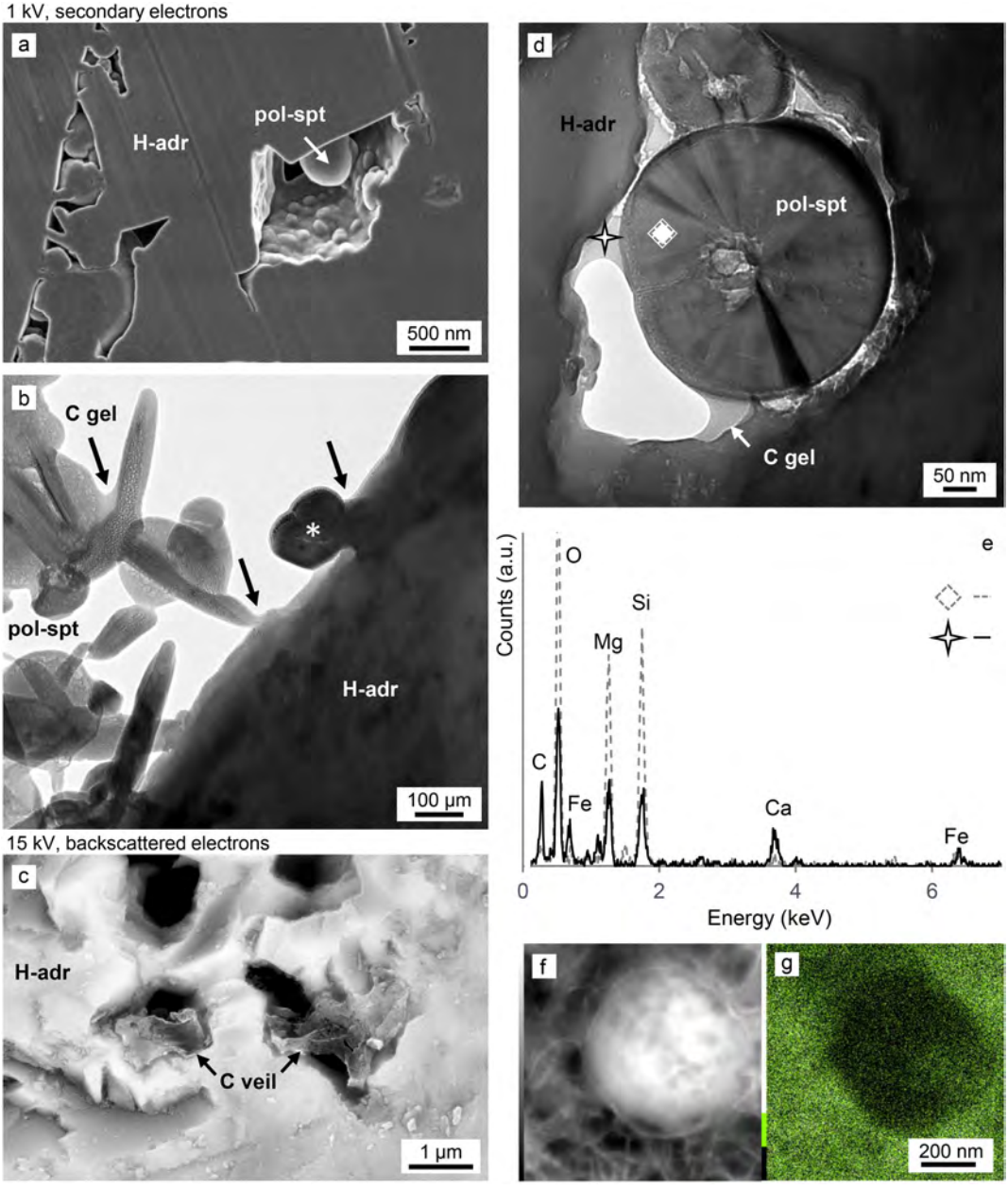
1 kV, secondary electrons
a
H-adr
pol-spt
500 nm
b
C gel
*
pol-spt
H-adr
100 µm
15 kV, backscattered electrons
c
H-adr
C veil
1 µm
d
H-adr
pol-spt
C gel
50 nm
e
Counts (a.u.)
O
Si
Mg
C
Fe
Ca
Fe
0
2
4
6
Energy (keV)
f
g
200 nm

Figure 5

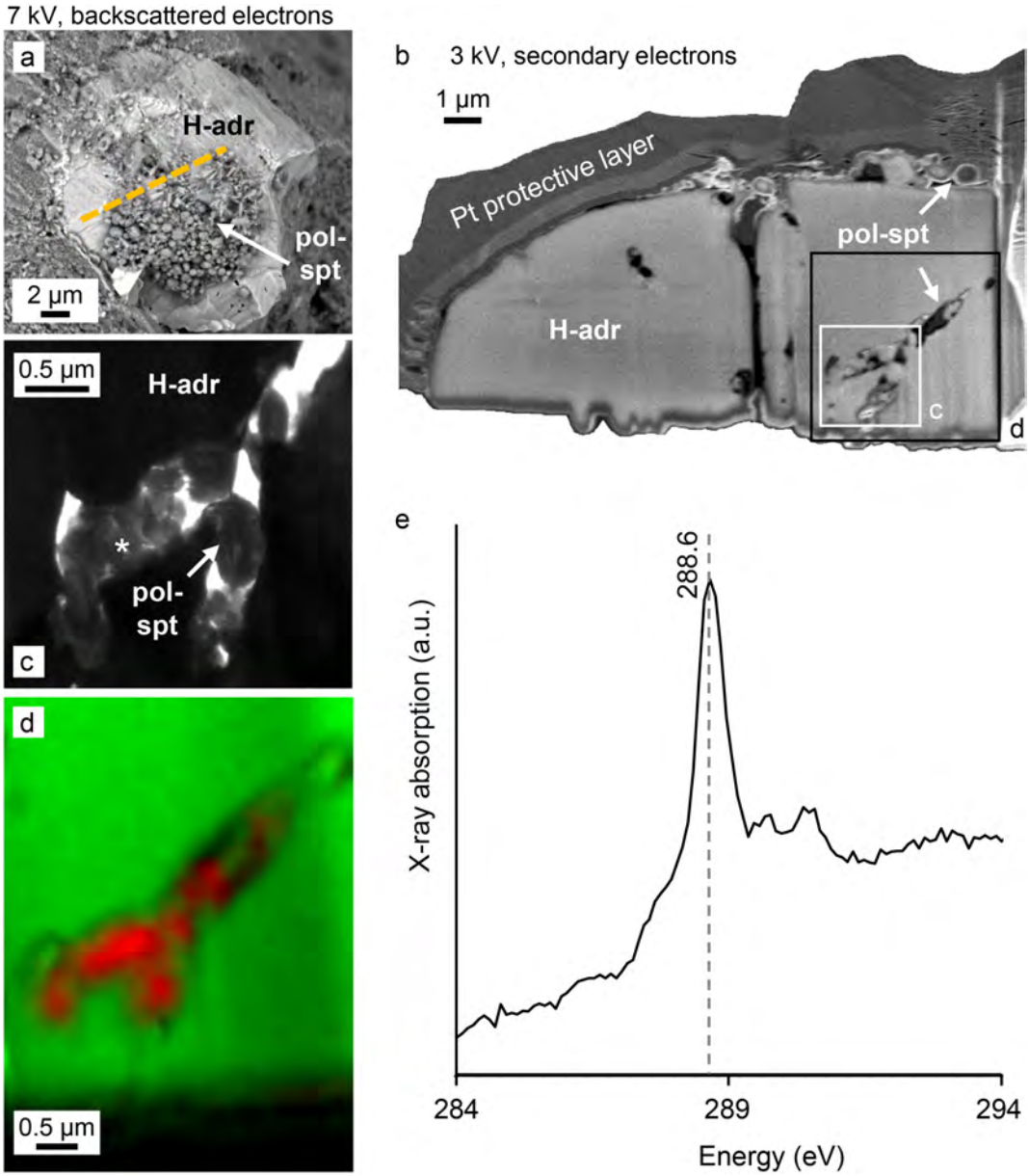
7 kV, backscattered electrons
a
H-adr
pol-
spt
2 µm
b
3 kV, secondary electrons
1 µm
Pt protective layer
pol-spt
H-adr
c
d
0.5 µm
H-adr
*
pol-
spt
c
d
0.5 µm
e
288.6
X-ray absorption (a.u.)
284
289
294
Energy (eV)

Figure 6

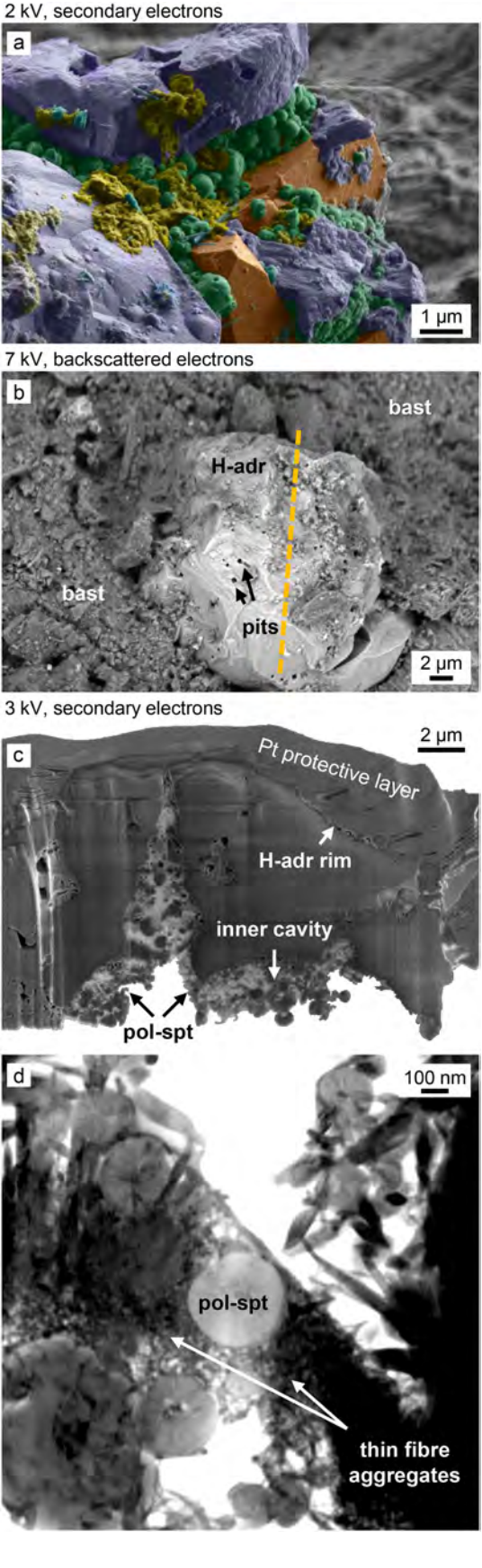
2 kV, secondary electrons
a
1 µm
7 kV, backscattered electrons
b
bast
H-adr
bast
pits
2 µm
3 kV, secondary electrons
c
2 µm
Pt protective layer
H-adr rim
inner cavity
pol-spt
d
100 nm
pol-spt
thin fibre aggregates

Figure 7

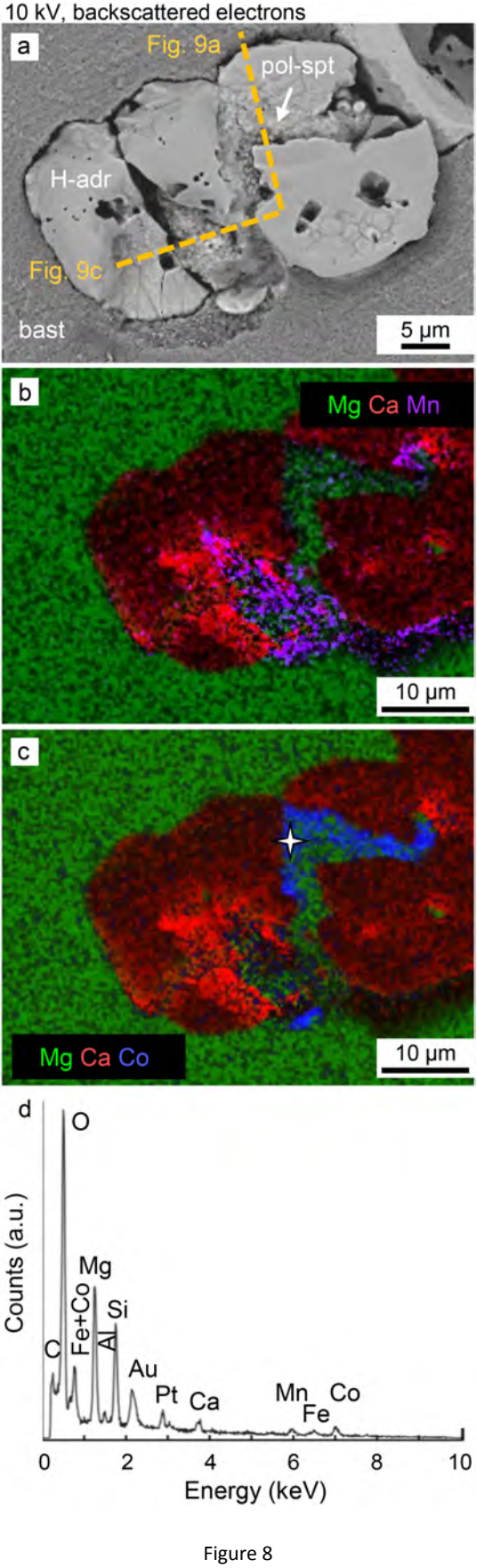
10 kV, backscattered electrons
a
Fig. 9a
pol-spt
H-adr
Fig. 9c
bast
5 µm
b
Mg Ca Mn
10 µm
c
Mg Ca Co
10 µm
d
O
Mg
Fe+Co
Si
C
Al
Au
Pt
Ca
Mn
Fe
Co
Counts (a.u.)
0
2
4
6
8
10
Energy (keV)

Figure 8

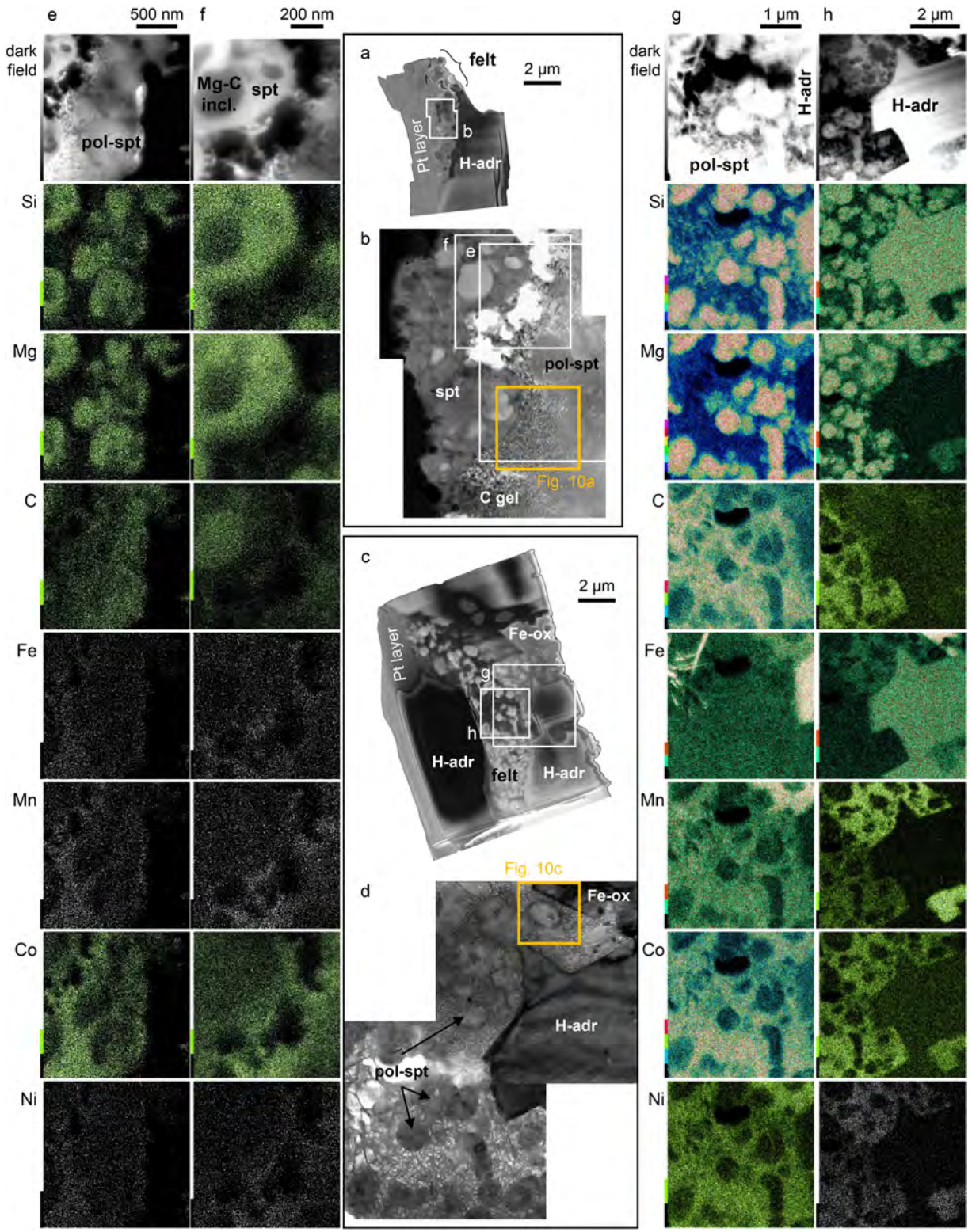
e
500 nm
f
200 nm
dark field
pol-spt
Mg-C incl.
spt
Si
Mg
C
Fe
Mn
Co
Ni
a
felt
2 µm
Pt layer
b
H-adr
b
f
e
pol-spt
spt
Fig. 10a
C gel
c
2 µm
Pt layer
Fe-ox
g
h
H-adr
felt
H-adr
Fig. 10c
d
Fe-ox
H-adr
pol-spt
g
1 µm
h
2 µm
dark field
H-adr
H-adr
pol-spt
Si
Mg
C
Fe
Mn
Co
Ni

Figure 9

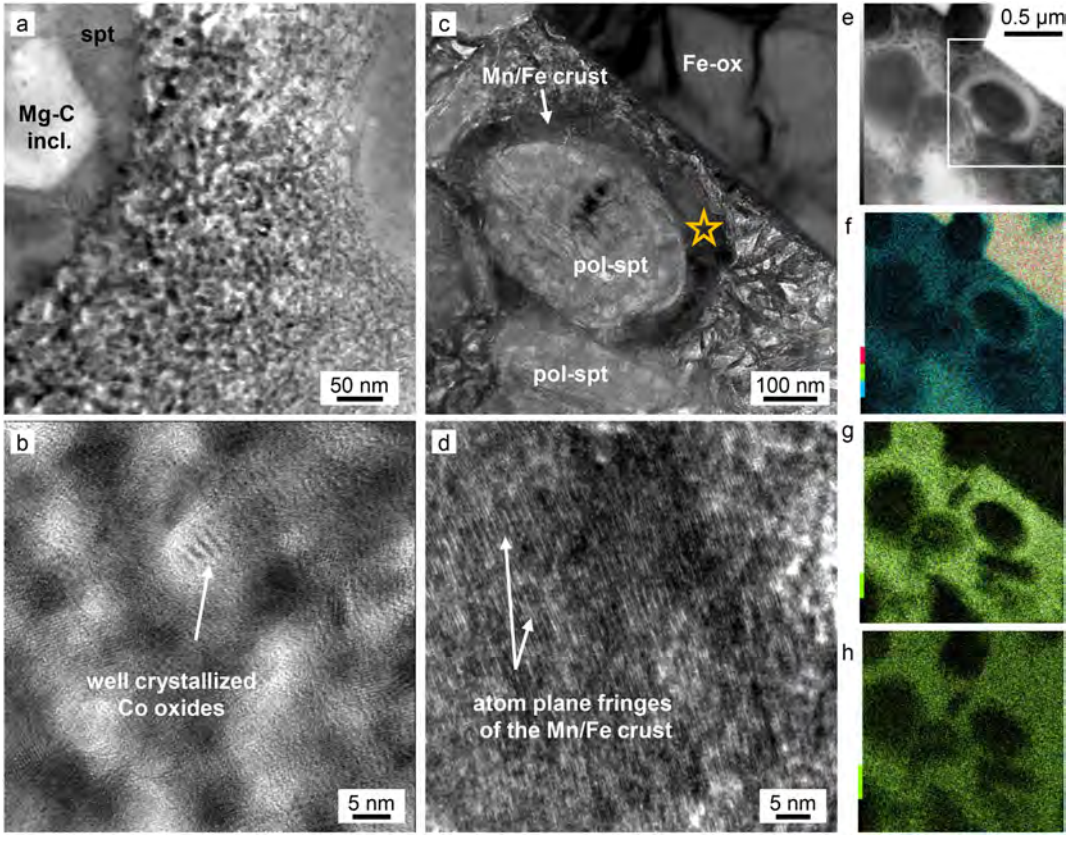
a
spt
Mg-C
incl.
50 nm
c
Mn/Fe crust
Fe-ox
pol-spt
pol-spt
100 nm
e
0.5 µm
f
b
well crystallized
Co oxides
5 nm
d
atom plane fringes
of the Mn/Fe crust
5 nm
g
h

Figure 10

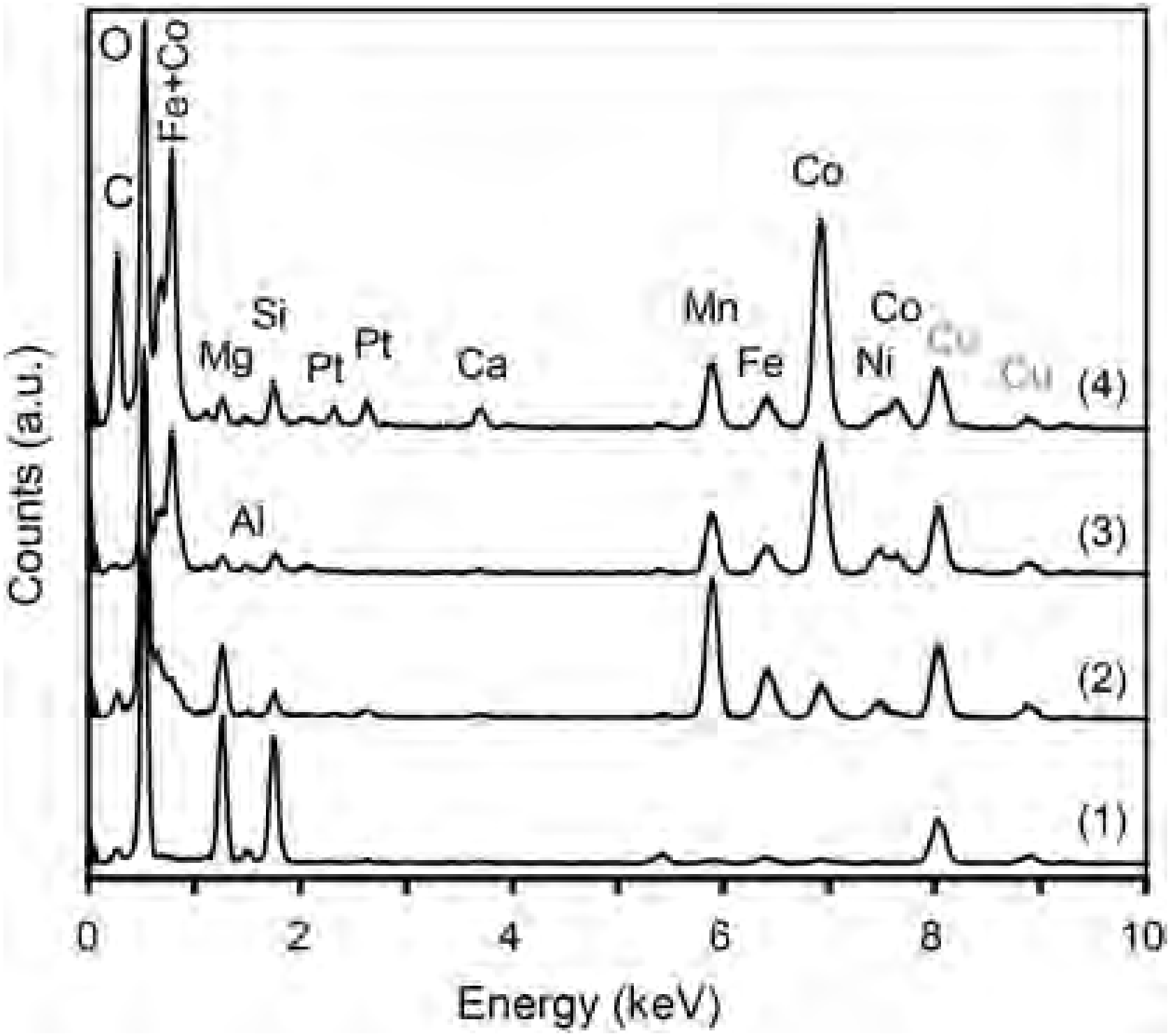
O
Fe+Co
C
Co
Si
Mn
Co
Mg
Pt
Pt
Ca
Fe
Ni
Cu
Cu
(4)
Al
(3)
(2)
(1)
Counts (a.u.)
0
2
4
6
8
10
Energy (keV)

Figure 11

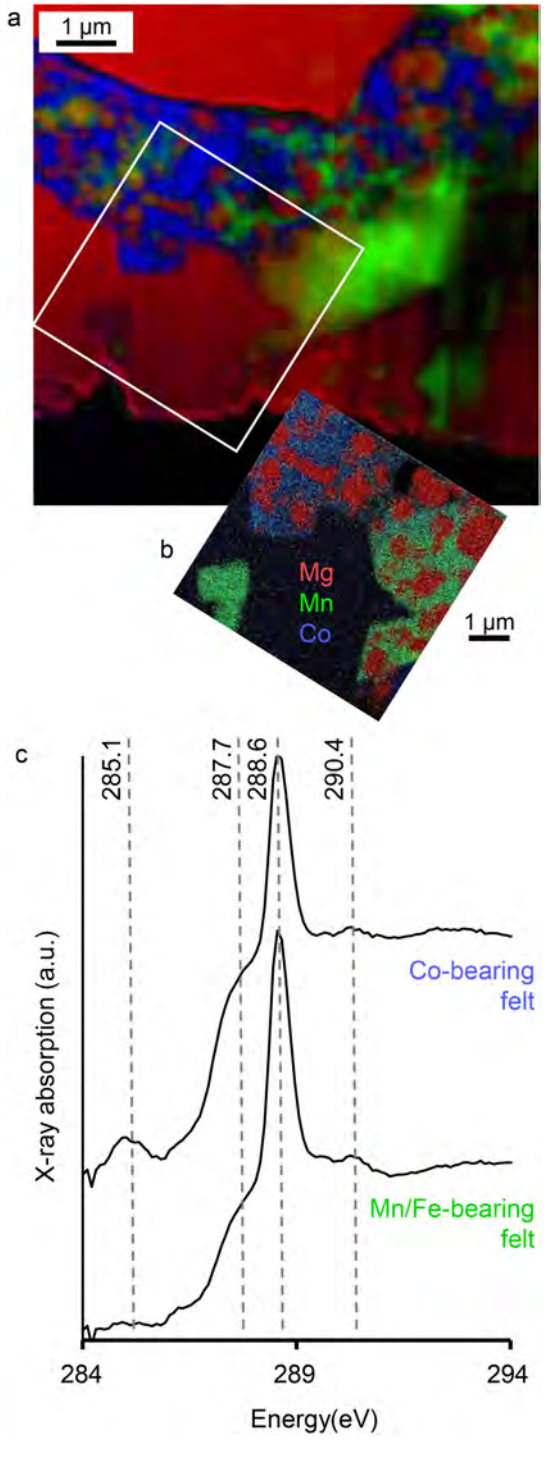
a
1 μm
b
Mg
Mn
Co
1 μm
c
285.1
287.7
288.6
290.4
X-ray absorption (a.u.)
Co-bearing felt
Mn/Fe-bearing felt
284
289
294
Energy(eV)

Figure 12